Received: 14 June 2016 | Accepted: 04 October 2017

DOI: 10.1111/gbi.12230

ORIGINAL ARTICLE

WILEY gebiology

A theory of atmospheric oxygen

T. A. Laakso | D. P. Schrag

Department of Earth and Planetary Sciences, Harvard University, Cambridge, MA, USA

Correspondence
T. A. Laakso, Harvard University Center for the Environment, Cambridge, MA, USA.
Email: laakso@fas.harvard.edu

Abstract

Geological records of atmospheric oxygen suggest that pO_2 was less than 0.001% of present atmospheric levels (PAL) during the Archean, increasing abruptly to a Proterozoic value between 0.1% and 10% PAL, and rising quickly to modern levels in the Phanerozoic. Using a simple model of the biogeochemical cycles of carbon, oxygen, sulfur, hydrogen, iron, and phosphorous, we demonstrate that there are three stable states for atmospheric oxygen, roughly corresponding to levels observed in the geological record. These stable states arise from a series of specific positive and negative feedbacks, requiring a large geochemical perturbation to the redox state to transition from one to another. In particular, we show that a very low oxygen level in the Archean (i.e., 10^{-7} PAL) is consistent with the presence of oxygenic photosynthesis and a robust organic carbon cycle. We show that the Snowball Earth glaciations, which immediately precede both transitions, provide an appropriate transient increase in atmospheric oxygen to drive the atmosphere either from its Archean state to its Proterozoic state, or from its Proterozoic state to its Phanerozoic state. This hypothesis provides a mechanistic explanation for the apparent synchronicity of the Proterozoic Snowball Earth events with both the Great Oxidation Event, and the Neoproterozoic oxidation.

1 | INTRODUCTION

The history of atmospheric oxygen can be divided into three broad periods, each with a characteristic level of oxygen in the atmosphere. During the Archean, pO_2 must have been less than 0.001% PAL to preserve mass independent fractionation of sulfur isotopes in the sedimentary record (Pavlov & Kasting, 2002). The lack of a mass-independent fractionation after 2.4 Ga indicates a more oxygenated Proterozoic, consistent with Paleoproterozoic changes in paleosol iron content (Rye & Holland, 1998), trace metal enrichments (Lyons Reinhard & Planavsky, 2014), and preservation of detrital pyrite and uraninite (Johnson, Gerpheide, Lamb, & Fischer, 2014). Proterozoic pO_2 remained below modern levels, with an upper bound of ~10% derived from sulfur isotope (Canfield & Teske, 1996) records. More recently, an upper bound of 0.1% PAL has been proposed based on chromium isotope data (Planavsky et al., 2014). In the late Neoproterozoic, the appearance of large-bodied animals (Anbar & Knoll, 2002) and an increase in trace metal enrichments (Lyons Reinhard & Planavsky, 2014) suggest a second rise in pO_2. Iron speciation is consistent with an increase in ocean oxygenation by the Devonian (Sperling et al., 2015), with the charcoal record requiring greater than 60% PAL since the Silurian (Scott & Glasspool, 2006).

Given these constraints, pO_2 may have varied by orders of magnitude within both the Archean and Proterozoic, and by a factor of two to six during the Phanerozoic. Whatever the variation, it is still clear that pO_2 remained within distinct, non-overlapping ranges during each eon, on timescales much longer than the residence time of any major redox-sensitive species in the ocean or atmosphere. During each eon, a system of negative feedbacks must have maintained pO_2 levels within the characteristic range of that eon. Several important negative feedbacks have been identified that may explain the stability of high pO_2 over the Phanerozoic (Bergman, Lenton, & Watson, 2004; Kump & Garrels, 1986; Lasaga & Ohmoto, 2002), but it is not obvious how these feedbacks are consistent with stability at multiple levels of pO_2 (Laakso & Schrag, 2014).

Much of the work on modeling atmospheric oxygen through Earth history has focused on explanations for these abrupt changes, rather than examining the reasons for stability of pO_2 either before or after the change. One hypothesis for the Great Oxidation Event (GOE) at

2.4 Ga is that it represents the beginning of biological oxygen production, which requires oxygenic photosynthesis to have evolved in the latest Archean (Kopp, Kirschvink, Hilburn, & Nash, 2005). Several lines of evidence, including sediment structures (Bosak, Knoll, & Petroff, 2013), trace metal enrichments (Anbar et al., 2007), and a number of isotopic systems (Farquhar, Zerkle, & Bekker, 2011), suggest oxygenic photosynthesis evolved hundreds of millions of years before the GOE, much longer than the residence time of any major redox species today. Such a long delay requires a mechanism for stabilizing oxygen at low levels in the presence of oxygenic photosynthesis, and an additional mechanism for driving the subsequent increase in oxygen at 2.4 Ga. Proposed mechanisms focus on long-term changes in oxygen consumption, driven by changes in the rate (Claire, Catling, & Zahnle, 2006) or oxidation state (Kump & Barley, 2007) of volcanic outgassing, or in the composition of the crust (Catling, Zahnle, & McKay, 2001). The Neoproterozoic oxidation event has been explained by invoking a step increase in the rate of oxygen production, driven by biological innovations that result in more efficient burial of organic carbon (Kennedy, Droser, Mayer, Pevear, & Mrofka, 2006; Logan, Hayes, Hieshima, & Summons, 1995).

These various hypotheses for what controls atmospheric O_2 have been difficult to test without a simple, mechanistic model of biogeochemical cycling that can elucidate the negative feedbacks responsible for the stability during any one eon, and determine whether a particular mechanism can overcome the negative feedbacks and transition from one steady state to another. In this paper, we describe a simple geochemical model of the redox cycles of iron, sulfur, hydrogen, oxygen, carbon, and phosphorous in the ocean and atmosphere. We investigate how the interactions between these cycles lead to dynamics that result in multiple steady states, even in the presence of oxygenic photosynthesis. The model is tuned to reproduce modern redox cycling in a three-box model with linear chemical kinetics. Our model is simple by intention and may not reproduce some details of modern redox cycling, which are important for controlling pO_2 within factors of two or more. For example, we do not include a land reservoir in the model nor terrestrial primary production, even though biogeochemical cycling of carbon on land today probably plays an important role in setting the equilibrium state. Such variations may be important in the context of redox changes through events in Earth history, such as the fourfold change in the Paleozoic inferred from iron speciation (Sperling et al., 2015), but are small in comparison with the very large changes in pO_2 (i.e., two orders of magnitude or more) between eons.

2 | MODEL & METHODS

Our model is a three-box representation of biogeochemical redox cycling in the atmosphere, the photic zone, and the deep ocean. It simulates the coupled cycles of oxygen, hydrogen, carbon, sulfur, and iron through primarily first-order kinetics. The dynamics are tuned to reproduce modern biogeochemical cycling (Table 1). A full description of the model is given the Supplementary Material, including tables of prognostic variables and the corresponding, time-dependent equations and flux parameterization (Tables S1-S3).

2.1 | Model description

Our model simulates the production, remineralization, export, and burial of organic matter. Organic matter and oxygen are produced via oxygenic photosynthesis in the photic zone, with a simplified stoichiometry of $CO_2 + H_2O \rightarrow CH_2O + O_2$. Production is P-limited, with an average biomass C:P ratio of 106:1. Production proceeds until there is complete uptake of bioavailable phosphate in the photic zone. Organic matter in the water column is remineralized through oxic respiration and sulfate reduction. Particles are deposited to the seafloor through direct and ballasted sinking. After deposition, organic matter is subject to remineralization by oxic respiration, iron and sulfate reduction, and methanogenesis. Remineralized phosphate is regenerated to the water column, at a rate that increases with decreasing oxygen (Colman & Holland, 2000).

CO_2 enters the ocean and atmosphere through volcanism, oxidative weathering of continental organic carbon, and weathering of terrestrial carbonates. Dissolved inorganic carbon (DIC) in the ocean exists as carbonic acid, bicarbonate ion, and carbonate ion in temperature-dependent equilibrium (Zeebe & Wolf-Gladrow, 2001), and exchanges with the atmospheric reservoir following a piston-velocity rate. DIC is removed from the ocean via precipitation of calcite and siderite. Precipitation and dissolution rates are proportional to the oversaturation, (Ω-1). Alkalinity is calculated from Fe^{2+} and SO_4^{2-} concentrations, modern Cl^- levels, and three additional cations: Ca^{2+}, Mg^{2+}, and the combination of Na^+ and K^+ (i.e., the other major cations not associated with carbonate). These cations enter the ocean via continental weathering. Mg^+, Na^+, and K^+ are removed via sinks proportional to their concentration in seawater. Magnesium removal is assumed to be via 1:1 hydrothermal calcium exchange, in which all of the Ca^{2+} is released to seawater. Calcium is removed via calcite precipitation and gypsum burial.

Phosphate enters the ocean/atmosphere system through apatite weathering and oxidative weathering of continental organic matter. Only a fraction of this flux is available for biological use; the remainder is detrital apatite, or is immobilized by scavenging onto mineral surfaces (Benitez-Nelson, 2000). The total supply of bioavailable phosphorus to the oceans, which we refer to as the "bioavailable phosphorus flux," is therefore controlled by two factors: the rate of apatite weathering, and the fraction of the weathered P which is available to biology.

The bioavailable fraction of apatite-derived P is oxygen sensitive. The availability increases by a factor of approximately 3 as pO_2 increases from 10% PAL to 100% PAL, plateauing at both higher and lower oxygen levels. The detailed parameterization is given in the Supplementary Material. This functional form represents changes in sorptive scavenging by iron under different redox conditions. Reduced forms of iron, which should be more prevalent in low-oxygen weathering environments (Holland, 1984), can be more efficient sinks for phosphate than ferric phases (Derry, 2015; Laakso & Schrag, 2014), suggesting the positive relationship used here. The asymptotic behavior at high and low oxygen levels reflects the switch from weathering environments completely dominated by ferrous iron, to those dominated by ferric iron.

	Modern	Anoxic	Low-O_2	High-O_2	Units
pO_2	0.0	−7.0	−1.9	−0.2	log PAL
P bioavailability	1.00	0.33	0.33	1.00	–
Organic burial	4.8	3.5	4.3	6.5	O_2
H_2 & CH_4 oxidation	−2.9	−0.0	−0.0	−1.8	O_2
Net Fe/S oxidation	0.6	−1.3	−2.1	−2.5	O_2
Pyrite weathering	−1.5	−1.4	−1.5	−1.5	O_2
H_2	−6.9	−7.7	−7.4	−7.0	Log mixing ratio
Volcanic, serpentinization	3.6	3.6	3.6	3.6	H_2
Pyrite formation	0.4	0.0	0.0	0.0	H_2
Oxidation	−4.0	−3.6	−3.6	−3.6	H_2
Escape	−0.0	−0.0	−0.0	−0.0	H_2
pCO_2	327	2182	3115	2865	ppm
Relative weathering rate	1.00	0.48	0.60	0.57	–
Volcanic, weathering	21.4	13.8	14.9	16.4	C
Organic burial	−4.8	−3.5	−4.3	−6.5	C
Siderite burial	−0.0	−2.2	−0.0	−0.0	C
Calcite burial	−16.6	−8.1	−10.6	−9.9	C
$[SO_4^{2-}]$	28.8	0.7	0.9	0.9	mM
Weathering, hydrothermal	3.7	0.8	0.9	0.9	S
Pyrite burial	−1.7	−0.2	−0.1	−0.1	S
Gypsum burial	−2.0	−0.6	−0.8	−0.8	S
$[Fe^{2+}]$	0.0	2.3	0.0	0.0	μM
Weathering, hydrothermal	4.5	3.0	3.3	3.3	Fe
Fe oxidation	−3.7	−0.7	−3.2	−3.3	Fe
Pyrite burial	−0.8	−0.1	−0.1	−0.0	Fe
Siderite burial	−0.0	−2.2	−0.0	−0.0	Fe
CH_4	−8.9	−9.0	−8.4	−9.0	Log mixing ratio
Methanogenesis	0.0	0.2	0.2	0.2	CH_4
Serpentinization	0.2	0.2	0.2	0.2	CH_4
Photolysis & oxidation	−0.0	−0.3	−0.3	−0.3	CH_4
AOM	−0.2	−0.1	−0.1	−0.1	CH_4

TABLE 1 Biogeochemical fluxes and reservoirs for representative steady-state conditions. The sinks for a particular species are listed as negative fluxes; sources are positive. Fluxes are given in units of Tmol y^{-1} for the given species. The modern simulation uses a combined H_2 + CH_4 outgassing flux of 4.4 Tmol H_2 y^{-1}, present-day solar luminosity, and includes sulfate weathering. The "anoxic," "low-O_2," and "high-O_2" states are simultaneously stable with identical boundary conditions: Each has a combined H_2 + CH_4 outgassing flux of 4.4 Tmol H_2 y^{-1}, no sulfate weathering, and 2.4 Ga solar luminosity. Pyrite weathering is a component of the net Fe/S cycling reported for the oxygen cycle

Such a relationship is required to explain the existence of low oxygen levels during the Proterozoic (Laakso & Schrag, 2014). As the limiting nutrient, the supply of bioavailable phosphorus must be balanced by the export of organic matter to sediments, at steady state. In the low-oxygen Proterozoic oceans, more efficient burial of this organic matter leads to a larger than modern source of oxygen, driving pO_2 back toward its modern equilibrium. However, if the flux of bioavailable phosphorus into the ocean were smaller during the Proterozoic, efficient burial of a small export flux could lead to no net increase in the oxygen source. A decrease in the supply of phosphorus under low-oxygen conditions can be explained as a decrease in the bioavailable fraction. Including this effect guarantees the model will have at least two stable levels of pO_2, and the parameterization is tuned to give stability at levels consistent with redox proxy records. This is not evidence for the effect, but allows us to explore an internally consistent model of biogeochemical cycling that can reproduce the large changes in oxygen recorded in the geological record.

Sulfur is divided between two reservoirs in our model, sulfate ion and hydrogen sulfide. Sulfate is reduced to sulfide via microbial sulfate reduction and anaerobic oxidation of methane (described in more

detail below), and re-oxidized by dissolved oxygen. Sulfur enters the ocean via the hydrothermal flux of hydrogen sulfide, weathering of sulfate minerals, and oxidative weathering of pyrite. Sulfur is removed through precipitation of gypsum and pyrite. Pyrite re-oxidizes at rate that decreases with rising O_2 concentrations, representing less efficient long-term burial in more oxidized settings (Westrich & Berner, 1984).

Ferrous iron enters the ocean system through hydrothermal systems and weathering of terrestrial silicate minerals. Dissolved ferrous iron may be oxidized to ferric iron by dissolved oxygen. All Fe^{3+} sinks to the sediment column, where it is available for microbial iron reduction. Siderite precipitation is described in detail in the discussion of carbon cycling, above.

Hydrogen enters the ocean/atmosphere system through volcanic outgassing and serpentinization. Atmospheric H_2 is lost through escape to space or oxidation in the ocean and atmosphere. We do not include oxidation of H_2 via reduction in ferric iron or sulfate. The oxidation kinetics of O_2 and H_2 are so rapid that even at the lowest oxygen concentrations simulated here, H_2 levels are extremely low (i.e., atmospheric mixing ratios of 100 ppb), so other pathways are assumed to be of secondary importance. Following Goldblatt, Lenton, and Watson (2006), net photochemical production and destruction of atmospheric H_2 are calculated using the two photochemical models described in Pavlov and Kasting (2002). The models' surface boundary conditions are fixed at various values of pO_2, pH_2 and pCH_4, then running to steady state, giving an approximation of the instantaneous net cycling of these three species as a function of atmospheric composition. See Supplementary Material for more detail. The hydrogen escape rate is calculated using the diffusion-limited rate given by Hunten (1973) for diffusion of hydrogen through air across a 200K homopause at 100 km. Typically, this calculation is based on the total hydrogen inventory at the homopause, assuming complete photolysis of methane and water vapor. Our model explicitly calculates H_2 concentrations in the homosphere, accounting for photochemistry as described above, and so we base our escape calculation only on H_2 mixing ratios. Further details are given in the Supplementary Material.

Methane is produced abiotically in serpentinizing systems, and through microbial methanogenesis. Methanogens consume organic matter following a simplified stoichiometry of $2CH_2O \rightarrow CO_2 + CH_4$. At each time step, this process consumes a fraction of the residual organic carbon not already remineralized by other forms of metabolism in the sediment. This fraction scales with the overall burial efficiency, simulating more rapid methanogenesis when more "labile" organic carbon is available to methanogens. The parameterization is tuned such that 10% of organic export is cycled through methanogenesis in the absence of other forms of remineralization, based on observations of ferruginous Lake Matano (Kuntz, Laakso, & Schrag, 2015). Dissolved methane is consumed through aerobic and anaerobic oxidation, with rates that scale with the concentrations of methane and either oxygen or sulfate, respectively. The net rate of methane oxidation in the atmosphere, $CH_4 + 2O_2 \rightarrow CO_2 + 2H_2O$, is calculated using the photochemical models described in Pavlov and Kasting (2002); the full procedure is described in the Supplementary Material.

Weathering includes oxidative and acidic processes. Oxidative weathering includes oxidation of continental organic carbon and pyrite. The rates are proportional to atmospheric pO_2. The pyrite oxidation rate is capped above a certain pO_2 level (10^{-7} PAL), in keeping with the disappearance of detrital pyrite grains in the Paleoproterozoic (Holland, 1984). Acidic weathering includes dissolution of apatite, carbonate, and silicate rocks, which releases iron, calcium, magnesium, sodium and potassium, and clays. This process scales with global surface temperature (Walker, Hays, & Kasting, 1981):

$$\omega = W(T)/W(T_0) = \exp\left(c_w \cdot (T - T_0)\right) \quad (1)$$

for a reference temperature T_0 and a relaxation scale c_w. Surface temperature is calculated relative to pre-industrial baselines for temperature (T_0) and atmospheric concentrations of both carbon dioxide ($p_{C,0}$) and methane ($p_{M,0}$):

$$T = T_0 \cdot L^{1/4} + \eta_C \log2(p_C/p_{C,0}) + \eta_M \cdot (p_M^{1/2} - p_{M,0}^{1/2}) \quad (2)$$

where L is the relative solar luminosity and the η terms are climate sensitivities. The parameterization of methane's radiative effects (Forster et al., 2007) assumes relatively low concentrations, which is consistent with all of our simulations (see Section 3).

2.2 | Steady-state simulations

We first simulate the modern biogeochemical cycle. The total hydrogen outgassing flux, including abiotic methane, is fixed at 4.4 Tmol H_2 y^{-1}, (see Canfield, Rosing, & Bjerrum, 2006; Holland, 2002), and solar luminosity is set to its present-day value. The model is initialized at approximately modern conditions and integrated forward for 15 million years. We next explore the range of stable states available to the model, integrated forward from a variety of initial conditions in pO_2. Each run is integrated for a minimum of 15 million years. To ease comparison between the resulting steady states, later Archean boundary conditions are used in all non-modern simulations: weathering of sulfate evaporates is not included (Grotzinger & Kasting, 1993) and the solar luminosity is fixed at its 2.4 Ga value. This process is repeated for a wide variety of hydrogen outgassing and serpentinization rates, given the uncertainty in these rates over Earth history. Greater heat loss from the early mantle was likely accommodated at least in part by more rapid seafloor spreading (Abbott & Hoffman, 1984), which may have limited serpentinization by restricting interaction between seawater and peridotites, which today occurs near very slow spreading ridges (Cannat, 1993). The high magnesium content of Archean basalts is consistent with more mafic crust, which could support much greater serpentinization rates, as in modern peridotite-hosted vents such as the Lost City or Rainbow fields. The net effect of these processes is uncertain, so we allow for a large range of hydrogen fluxes.

2.3 | Simulation of Snowball glaciation

Global or "Snowball" glaciation is believed to occur when a runaway ice–albedo feedback leads to ice cover reaching nearly to the equator.

A combination of low temperatures and extensive ice cover allows volcanic CO_2 to accumulate in the atmosphere until melting begins. The ice–albedo feedback operates in reverse, driving rapid retreat of the ice sheet. Silicate weathering rates are very rapid in the ice-free, CO_2-rich "hothouse" environment that follows, producing characteristic cap carbonates and bringing the carbon cycle back into equilibrium (Hoffman, Kaufman, Halverson, & Schrag, 1998). We examine the impact of glaciation on global redox chemistry by imposing ice cover on our geochemical cycling model. pCO_2 evolves according to the altered chemical dynamics, and the ice cover is removed once pCO_2 reaches a predefined melting threshold. These simulations are not intended to address the conditions that initiate glaciation, or the carbon dioxide level at which melting occurs, but to examine the response of pO_2 to a Snowball glacial episode.

During glaciation, sea-ice cover reduces the surface area of the open ocean to some fraction, f_{sea}, of its modern value, restricting air–sea gas exchange, and reducing the volume of the photic zone by the same fraction. Mixing between the photic zone and the rest of the ocean is assumed to be dominated by lateral advection from ice-covered surface waters, at a rate M_g. Land ice cover slows weathering by limiting contact between the continents and the atmosphere. During glaciation, the oxidative weathering rate at a given value of pO_2 is reduced to some fraction, f_{ox}, of its non-glacial rate. Acidic weathering rates are affected by both the ice cover and the change in temperature at weathering sites. Given the challenge of simulating surface temperatures using our simple climate parameterization, glacial weathering rates instead scale weakly with pCO_2 itself, relative to the weathering rate at 0°C:

$$\omega_{glacial} = \exp\left(c_g \cdot \log_2\left(pCO_2\right)\right) \cdot \omega_{(T=0)} \quad (3)$$

The bioavailability of weathered apatite may also change in an environment with large contributions from subglacial weathering. We experiment with a range of oxygen-independent, intraglacial values for the bioavailable fraction, b. Following deglaciation, rapid weathering of finely ground glacial till will result in large sediment loads that may efficiently adsorb dissolved phosphorus. We suppress the bioavailable fraction to a new value, b_m, at the time of deglaciation, which relaxes linearly back to its oxygen-sensitive unglaciated value over a period τ.

Individual simulations begin from one of the steady states of the unglaciated model. Glacial conditions are imposed instantaneously, and the model is integrated forward until the pCO_2 melting threshold is reached, when fully unglaciated conditions are restored, with the exception of the bioavailable fraction which relaxes to its unglaciated value as described above. Individual simulations are characterized by a choice of the pCO_2 threshold for melting; the intraglacial phosphate bioavailability b; and the post-glacial bioavailability relaxation timescale τ. Other glacial parameters were not varied between runs, including the fraction of open ocean area f_{sea} (0.001); the ratio of glacial:non-glacial oxidative weathering rates f_{ox} (0.1); the strength of the intraglacial silicate weathering feedback c_g (−0.44); the post-melting bioavailability b_m (0.1); and the photic zone mixing rate M_g (1.9 Sv, derived from a horizontal surface current of 10 cm/s flowing into photic zones underlying circular holes).

2.4 | Secular decline in hydrogen outgassing

Following Canfield (2004), we simulate a secular decline in the rate of hydrogen outgassing rate, $F_{H,}$ by letting it scale with the square of mantle heat flow, using a quadratic fit to the heat flow estimates of Turcotte (1980):

$$F_H(t) = (1 + 0.1217 \cdot t + 0.0942 \cdot t^2)^2 \cdot F_H(t=0) \quad (4)$$

where t is the time before present in billions of years. The rate of change is accelerated by a factor of 10; this allows the integration time to be computationally tractable, while allowing the rate of change in F_H to remain slow relative to the relaxation time of the biogeochemical system. The resulting rates of change in pO_2 should therefore be taken as a maximum. The integration begins at the Archean steady state described below, with t = 2.4 Ga, and F_H (t = 0) chosen such that the flux at that time is 4.4 Tmol H_2 y^{-1}.

3 | RESULTS

3.1 | Modern biogeochemical cycling

The output from our model with modern boundary conditions is summarized in Table 1. Equilibrium pO_2 is 1.0 PAL. The primary source of oxygen is 4.8 Tmol O_2 y^{-1} of organic carbon burial, with an additional 0.6 Tmol O_2 y^{-1} from net sulfur and iron cycling, dominated by net burial of pyrite. The compensating sink is 2.9 Tmol O_2 y^{-1} of organic carbon weathering and 2.2 Tmol O_2 y^{-1} of net hydrogen oxidation.

Sulfate concentrations are 28.8 mM. The total flux of sulfur to the ocean is 3.7 Tmol S y^{-1}. Approximately 20% of this flux is derived from pyrite oxidation and the remainder from evaporite weathering. Sulfur burial is approximately 45% pyrite and 55% sulfate minerals. Dissolved iron concentrations are less than 1 nM; iron derived from weathering and hydrothermal input is removed primarily through oxidation, with the remaining 20% removed as pyrite.

Equilibrium pCO_2 is approximately 330 ppm, given an average surface temperature of 15°C. pCO_2 stabilizes above pre-industrial levels of 280 ppm due to very low equilibrium levels of methane, approximately 1 ppb compared with the estimated pre-industrial value of 600 ppb. The production of alkalinity via weathering is tuned to balance the carbon cycle at a temperature of 15°C; in the absence of any appreciable methane greenhouse effect, this equilibrium is only achieved at 330 ppm pCO_2.

Methane levels are low in our model due to the lack of a terrestrial biosphere model. Today, the vast majority of non-anthropogenic methane is produced in terrestrial wetlands, with the ocean source representing at most a few percent of the flux to the atmosphere (Reeburgh, 2007). Abiotic production of methane during serpentinization is the largest source of methane in our modern model, and this is largely lost to AOM before outgassing to the atmosphere. This simplified model limits our ability to perfectly reproduce the modern, but should apply before the development of modern land plants, and the associated weathering and primary production regimes, in the Devonian. This allows for an internally consistent model across the Archean, Proterozoic, and the Paleozoic.

3.2 | Steady states of the surface redox cycle

The atmosphere stabilizes at a different level of pO_2 depending on the initial state of the atmosphere. The steady-state levels of pO_2 are summarized Figure 1. The number and value of these equilibrium levels varies as a function of the hydrogen input flux, but at least two states are simultaneously stable for hydrogen fluxes between 2 and 4 Tmol H_2 y^{-1}. The evolution of pO_2 to its steady-state values is shown in Figure 2; three different hydrogen fluxes are assumed, demonstrating the differences in steady states available to the atmosphere under different outgassing conditions.

The steady states can be grouped into three categories based on oxygen level: pO_2 less than 10^{-7} PAL, pO_2 between 10^{-4} and 10^{-1} PAL, and pO_2 greater than 40% PAL. A representative biogeochemical budget for each of these states is given in Figure 3 and Table 1.

3.2.1 | Anoxic Earth: $pO_2 < 10^{-7}$

The lowest oxygen state has pO_2 less than 10^{-7} PAL. Here, we describe the budget for a hydrogen flux of 4.4 Tmol H_2 y^{-1}. The bioavailability of weathering-derived phosphorus is ~30% of its modern value, due to the low level of pO_2. The small supply of bioavailable phosphorus from rivers, combined with inefficient remineralization of organic P, supports only 4 Tmol C y^{-1} of primary production. Efficient burial of this small pool of organic matter gives an oxygen source of 3.5 Tmol O_2 y^{-1}, or 70% of the modern value.

The compensating oxygen sink is net oxidation of hydrogen, iron, and sulfur. The rapid kinetics of H_2 oxidation result in complete oxidation of the H_2 input from volcanoes and serpentinization, consuming 2.2 Tmol O_2 y^{-1}. Oxidation of sulfide and pyritic sulfur, followed by burial of sulfate minerals, consumes 1.1 Tmol O_2 y^{-1}. Oxidation of iron, followed by removal as ferric oxides, consumes 0.2 Tmol O_2 y^{-1}, closing the oxygen budget.

Sulfur enters the oceans through hydrothermal systems, at a rate of 0.1 Tmol S y^{-1}, and through oxidative weathering of pyrite. Atmospheric oxygen is too low to weather continental pyrite to completion; of the 0.8 Tmol pyritic sulfur exposed annually by erosion, 0.7 Tmol are oxidized to sulfate. 0.7 Tmol S y^{-1} is ultimately buried as sulfate minerals, with the remaining 0.2 Tmol precipitating as pyrite. Hydrogen sulfide and sulfate concentrations are 7.9 μM and 0.7 mM, respectively.

Iron enters the ocean through hydrothermal systems and weathering of pyrite and silicate minerals, at a rate of 3.0 Tmol Fe y^{-1}. Pyrite burial is limited by the availability of sulfide and removes 0.1 Tmol Fe y^{-1}. Iron oxides and siderite precipitate at rates of 0.7 and 2.2 Tmol Fe y^{-1}. Ferrous iron concentrations are 2.3 μM.

Carbon inputs from volcanic outgassing and carbonate weathering are balanced by burial of 3.5 Tmol C y^{-1} organic matter, 2.2 Tmol C y^{-1} siderite, and 8.1 Tmol C y^{-1} calcium carbonate. pCO_2 equilibrates at 2164 ppm.

Atmospheric methane levels are approximately 1 ppb. Methanogenesis is very efficient in the oxygen- and sulfate-poor environment, remineralizing 9% of primary production, equivalent to the methanogenesis rates observed in ferruginous Lake Matano (Kuntz et al., 2014). However, total production is less than 1% of the terrestrial source today (Reeburgh, 2007). This source of methane is sufficiently small that photo-oxidation, even in a low-oxygen atmosphere, balances the methane budget at equilibrium levels of only a few parts per billion.

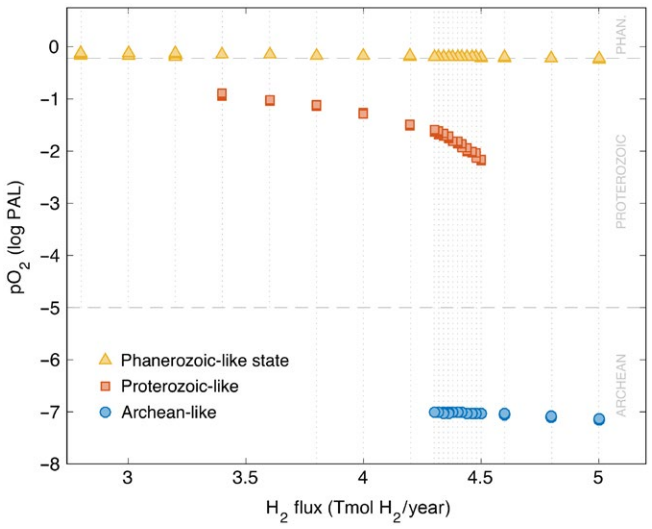

FIGURE 1 Steady-state pO_2 for various values of the hydrogen input flux, at Archean solar luminosity. For a given value of the hydrogen flux, as many as three steady states may be simultaneously stable, with steady equilibrium values of pO_2 consistent with the proxy records of the Archean, Proterozoic, and Phanerozoic. Associated phosphorus and iron fluxes for each steady state are shown in the Supplementary Material [Colour figure can be viewed at wileyonlinelibrary.com]

3.2.2 | Low-oxygen Earth: 10^{-3} PAL < pO_2 < 10^{-1} PAL

The intermediate-oxygen state has a range of pO_2 values between 10^{-3} and 10^{-1} PAL. For a hydrogen input flux of 4.4 Tmol O_2 y^{-1}, pO_2 is $10^{-1.9}$ PAL. Relative to the anoxic state, the supply of bioavailable phosphate increases by approximately 20%, due to changes in carbon and iron cycling that occur at larger oxygen levels, as described below. The increase in phosphate is balanced by a 20% (0.8 Tmol O_2 y^{-1}) increase in organic carbon burial, to 4.3 Tmol O_2 y^{-1}. At steady state, the increase in oxygen production is balanced by an increase in net oxidation of sulfur (0.2 Tmol O_2 y^{-1}) and iron (0.6 Tmol O_2 y^{-1}).

Continental pyrite is oxidized to completion, increasing the flux of riverine sulfate by 0.1 Tmol S y^{-1} relative to the anoxic state. Gypsum burial increases by 0.2 Tmol S y^{-1}, while pyrite precipitation falls by 0.1 Tmol S y^{-1}. Sulfate and sulfide concentrations are 0.9 mM and 0.7 nM. More than 95% of ferrous iron input is balanced by ferric oxide precipitation. Ferrous iron concentration is 6.0 nM. Siderite burial ceases in the ferrous-iron-poor environment.

Steady-state pCO_2 is 3115 ppm, approximately 1000 ppm higher than in the anoxic state. The associated increase in global temperature drives more rapid silicate weathering, increased alkalinity, and ultimately more rapid precipitation of calcite. The increase in temperature

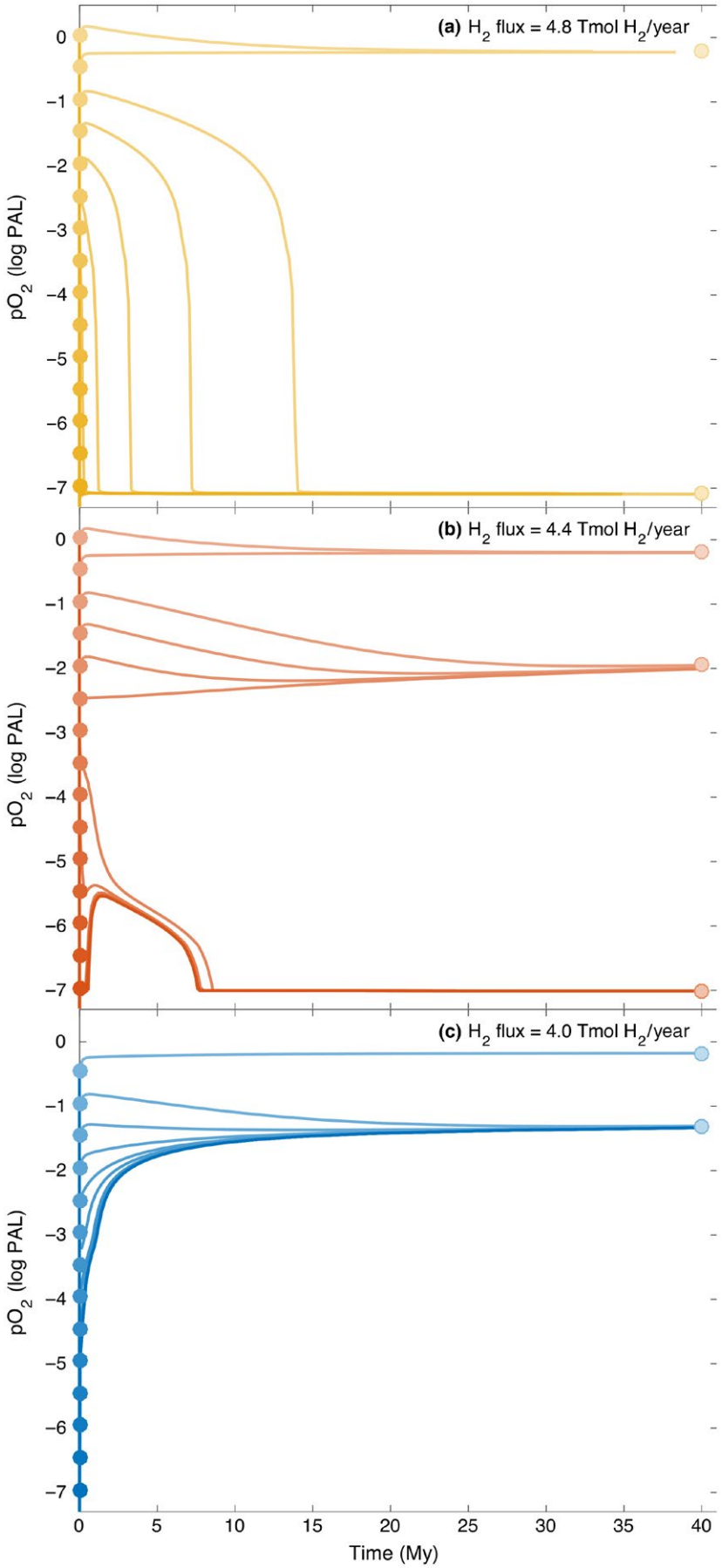

FIGURE 2 Evolution of atmospheric pO_2 from various initial conditions for hydrogen outgassing fluxes of 4.8 (a), 4.4 (b), and 4.0 (c) Tmol H_2 y^{-1}. The number and value of the equilibrium levels of pO_2 varies as a function of the hydrogen flux [Colour figure can be viewed at wileyonlinelibrary.com]

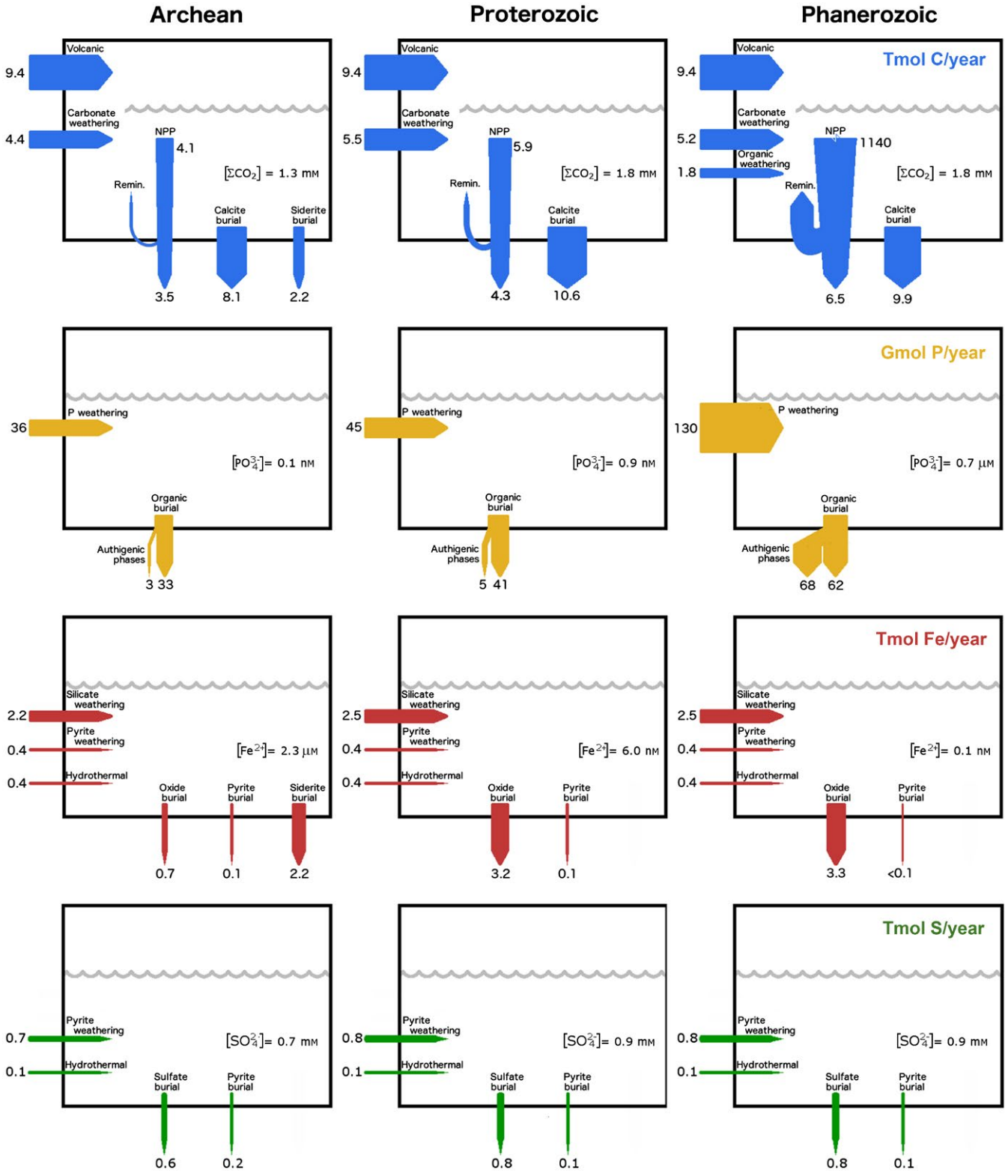

FIGURE 3 Biogeochemical fluxes of iron, sulfur, carbon, and bioavailable phosphorus under steady-state conditions. The three steady states have identical boundary conditions: an H_2 flux of 4.4 Tmol H_2 y^{-1}, no sulfate weathering, and 2.4 Ga solar luminosity. The different equilibrium conditions result from initializing the model under different conditions. Though the solar luminosity is not appropriate for a Phanerozoic simulation, this allows the states to be compared directly. Full geochemical budgets, including oxygen and hydrogen fluxes, are given in Table 1. Concentrations are given for the deep ocean. Burial fluxes are the sum of burial in deep- and shallow-water sediments. In the Phanerozoic state, the calcite weathering term includes a contribution from organic carbon weathering [Colour figure can be viewed at wileyonlinelibrary.com]

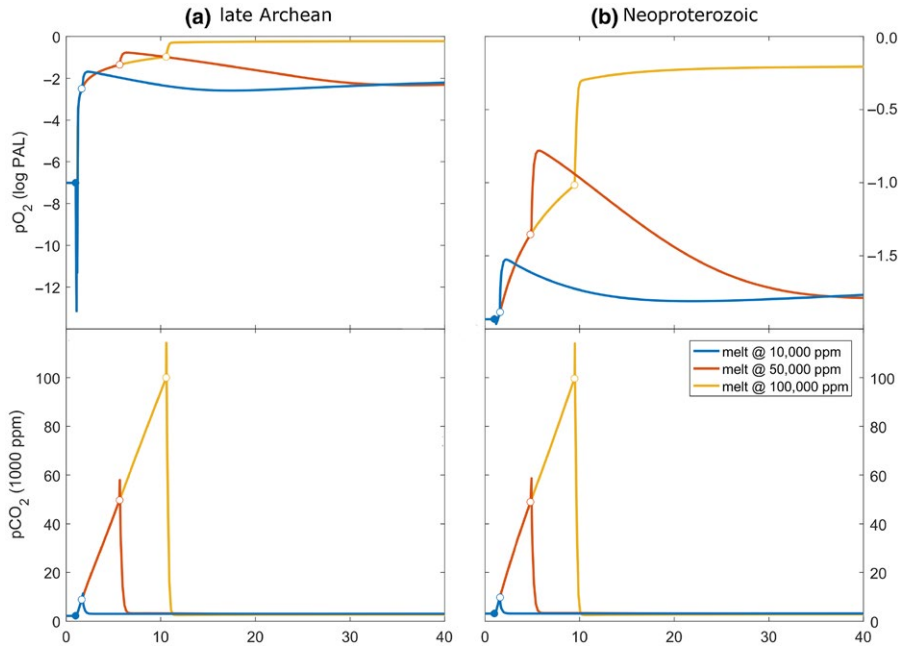

FIGURE 4 Evolution of atmospheric pO_2 (top) and pCO_2 (bottom) through possible Snowball Earth events in the late Archean (a) and Neoproterozoic (b). Each curve corresponds to a simulation with a different pCO_2 threshold for glacial termination. The glacial begins at 1 million years (closed circle), and ends (open circle) when pCO_2 reaches the specified melting threshold. The full simulation parameters are given in Section 3.2. For sufficiently high melting thresholds, the perturbation associated with the glaciation drives a permanent transition from one steady-state level of oxygen to another [Colour figure can be viewed at wileyonlinelibrary.com]

also affects the apatite weathering rate. The bioavailable fraction of weathered P is nearly identical between the low- and intermediate-oxygen states. However, the increase in weathering itself leads to an additional flux of 7.5 Gmol bioavailable P y^{-1}. This input is balanced by an increase in organic matter burial, equivalent to 0.8 Tmol C y^{-1}. This is the additional source of oxygen referenced above and, with the increase in calcite precipitation, balances the 2.2 Tmol C y^{-1} decrease in siderite precipitation.

3.2.3 | High-oxygen Earth: pO_2 > 40% PAL

The high-oxygen state has steady-state pO_2 of 60% PAL. This state includes the modern simulation, but encompasses a wider range of pO_2 values, given possible variations in boundary conditions such as the solar luminosity, sulfur evaporate weathering, and H_2 outgassing fluxes.

This is sufficiently oxidizing to support modern levels of phosphorus bioavailability, 3.5 times the bioavailability in the low- or intermediate-oxygen states (see Section 2). The resulting source of oxygen from organic carbon burial is 6.5 Tmol O_2 y^{-1}, much larger than in either of those cases.

Oxidative processes dominate the cycles of hydrogen, sulfur, and iron. Hydrogen inputs are balanced entirely by oxidation, consuming 2.2 Tmol O_2 y^{-1}. Net oxidation of iron and sulfur removes 0.8 and 1.7 Tmol O_2 y^{-1}. Weathering of organic carbon, which was insignificant in the low- and intermediate-oxygen cycles, consumes an additional 1.8 Tmol O_2 y^{-1}.

Iron from weathering and hydrothermal systems is removed overwhelmingly as iron oxides at a rate of 3.3 Tmol Fe y^{-1}; pyrite accounts for only 1% of the sink, and siderite does not precipitate. Continental pyrite weathers to completion, for a total flux of 0.9 Tmol S y^{-1}. 0.8 Tmol S is buried as gypsum and 0.1 Tmol S as pyrite.

pCO_2 stabilizes at 2865 ppm, approximately 150 ppm lower than the intermediate-oxygen state. The relative decrease in pCO_2 slows the flux of alkalinity, reducing calcium carbonate burial by 0.6 Tmol C y^{-1}. This compensates for the increase in net organic carbon burial associated with the oxygen-mediated increase in phosphate bioavailability.

3.3 | Evolution of pO_2 during Snowball glaciation

Figure 4 (a) shows the evolution of pO_2 and pCO_2 through simulations of a Paleoproterozoic Snowball Earth event. The biogeochemical cycle is initialized at its low-oxygen, Archean-like state ($pO_2 \sim 10^{-7}$ PAL), with a 2.4 Ga solar luminosity and a hydrogen flux of 4.4 Tmol H_2 y^{-1}. During the glacial, phosphorus bioavailability b is fixed at its modern value. Bioavailability returns to its unglaciated, oxygen-determined value immediately after deglaciation ($\tau = 0$). Melting occurs when pCO_2 reaches a "melting threshold," which varies between simulations.

Prior to glaciation, the oxygen budget of the atmosphere is balanced between outgassing of photosynthetic O_2 from the photic zone, and oxidation of atmospheric H_2 and subaerial pyrite. The oxygen sensitivity of the pyrite oxidation rate stabilizes pO_2 against transient fluctuations.

When glaciation begins, silicate and apatite weathering rates decrease due to ice cover and a drop in temperature. This leads to an immediate decrease in the supply of bioavailable phosphorus, depressing both the gross photosynthetic production of O_2, and surface water oxygen concentration. The decline in surface water [O_2], coupled to a

drop in the area of the open ocean, causes the rate at which oxygen diffuses into the atmosphere to drop by more several orders of magnitude. Oxygen levels fall immediately to less than 10^{-10} PAL.

The decrease in the volume of the photic zone is accompanied by an immediate, proportional decrease in primary production. This decrease is much larger than the decrease in the bioavailable phosphorus flux. Phosphorus accumulates in the ocean, raising its concentration until advection into the photic zone becomes rapid enough to drive the organic matter production required to balance the P budget. The highly concentrated primary production increases photic zone O_2 concentration, causing a recovery of the outgassing rate over several hundred thousand years. This rate does not recover to its pre-glacial level, but it eventually exceeds the maximum rate of oxidative weathering that is possible given the land ice cover. The source of oxygen therefore exceeds the maximum sink, and atmospheric pO_2 begins to rise.

Oxygen continues to rise throughout the glacial period. In this simulation, pCO_2 reaches the melting threshold after approximately 5 million years, during which time oxygen has risen to ~10^{-2} PAL, an increase of five orders of magnitude.

After deglaciation, elevated pCO_2 and an ice-free albedo result in very high temperatures, and a more than 10-fold increase in the release of bioavailable phosphorus to the oceans. The result is net production of O_2 during the period of rapid weathering. pO_2 increases by an order of magnitude in less than 500,000 years, while pCO_2 declines back toward its equilibrium value.

The high oxygen level depresses iron concentrations in the ocean, stopping siderite precipitation, which removed 2.2 Tmol C y^{-1} before the glacial period. Without this sink, pCO_2 remains slightly elevated, providing the additional silicate weathering required to compensate for the lost siderite with additional calcite burial. Elevated pCO_2 also accelerates apatite weathering, providing the increase in phosphate weathering required to maintain high oxygen levels. This configuration of the biogeochemical cycle is stable (see Section 3.2), allowing pO_2 to relax permanently to its Proterozoic state, with oxygen levels of 10^{-2} PAL.

The simulations in Figure 4 (b) correspond to possible Neoproterozoic Snowball events. The biogeochemical cycle is initialized at its low-oxygen, Proterozoic-like state (in our model, pO_2 of ~10^{-2}). The overall trajectory of pO_2 is similar to the Paleoproterozoic case. The early, transient drop in pO_2 is relative small due to the larger baseline reservoir of oxygen. pO_2 rises by approximately an order of magnitude during the glacial period, and by another order of magnitude in the post-glacial hothouse. This transient increase in pO_2 drives an increase in the bioavailability of phosphate, stabilizing the atmosphere at this more oxidizing condition. The biogeochemical cycle relaxes to its Phanerozoic equilibrium state, with oxygen levels above 60% PAL.

3.4 | Sensitivity to the glacial melting threshold

The evolution of pO_2 through Snowball events in which melting occurs at different levels of pCO_2 is shown in the Supplementary Material. All other glacial parameters are held at the values described in the previous section.

For the Paleoproterozoic, oxygenation occurs even for a pCO_2 melting threshold as low as 10,000 ppm. In order to relax to the Proterozoic state, pO_2 needs to rise high enough to suppress ferrous iron concentrations and siderite precipitation. This threshold is easily reached even for short glacial periods, as the total oxygen content of the atmosphere is small, allowing pO_2 to reach approximately Proterozoic levels in less than 1 million years. If the Snowball persists long enough (melting at 80,000 ppm or more), pO_2 rises above 10^{-1}, the level at which phosphorus bioavailability increases dramatically (Methods). In this case, pO_2 bypasses the Proterozoic equilibrium state entirely, and jumps immediately to a Phanerozoic steady state after the glacial.

In the Neoproterozoic Snowballs, pO_2 collapses back to its Proterozoic steady state if the melting threshold is below 90,000 ppm. Oxygenation to the Phanerozoic state requires pO_2 to be pushed above 10^{-1}, when P bioavailability rises. Although this is a smaller relative increase in pO_2 than in the Archean–Proterozoic transition, it is much larger in an absolute sense, and more time is required to pump sufficient oxygen into the atmosphere. The actual value of these thresholds is a product of our parameterizations of weathering rates, and could be substantially different in the real world. The existence of an oxygenation threshold for each Snowball event is the more significant finding.

3.5 | Sensitivity to the glacial bioavailability of phosphate

The evolution of pO_2 through Paleoproterozoic Snowball events with varying phosphorus bioavailability is shown in the Supplementary Material. The baseline case has bioavailability fixed at 75% of modern during glaciation. After the glaciation ends, bioavailability rebounds immediately to its oxygen-sensitive level ($\tau = 0$). Melting occurs at 10,000 ppm pCO_2.

First, we consider the effect of varying the P bioavailability during the glacial event. pO_2 does not increase during the glacial period itself if the bioavailability of P is depressed to 60% of modern during the glaciation. Although this still represents an increase in bioavailability relative to the pre-glacial state, the decrease in total apatite weathering is large enough to offset this change, and the total bioavailable phosphorus flux declines more than the rate of oxidative weathering. O_2 is unable to accumulate in the atmosphere under these conditions. However, the post-glacial pulse of oxygen production is so large that the atmosphere still transitions to its Proterozoic state once the glaciation is complete.

We also consider the effect of suppressing phosphorus bioavailability immediately after deglaciation. In this experiment, bioavailability is suppressed to 10% of modern, then relaxes back to its oxygen-controlled level (~30%) over a timescale τ. If the combination of the decreased bioavailability and increased apatite weathering leads to an overall decrease in the bioavailable flux relative to steady state, pO_2 falls. For τ = 100,000 years, the bioavailable flux is only transiently depressed, and oxygen levels rebound to the Proterozoic state after a short dip. For τ = 500,000 years, oxygen is forced back to its

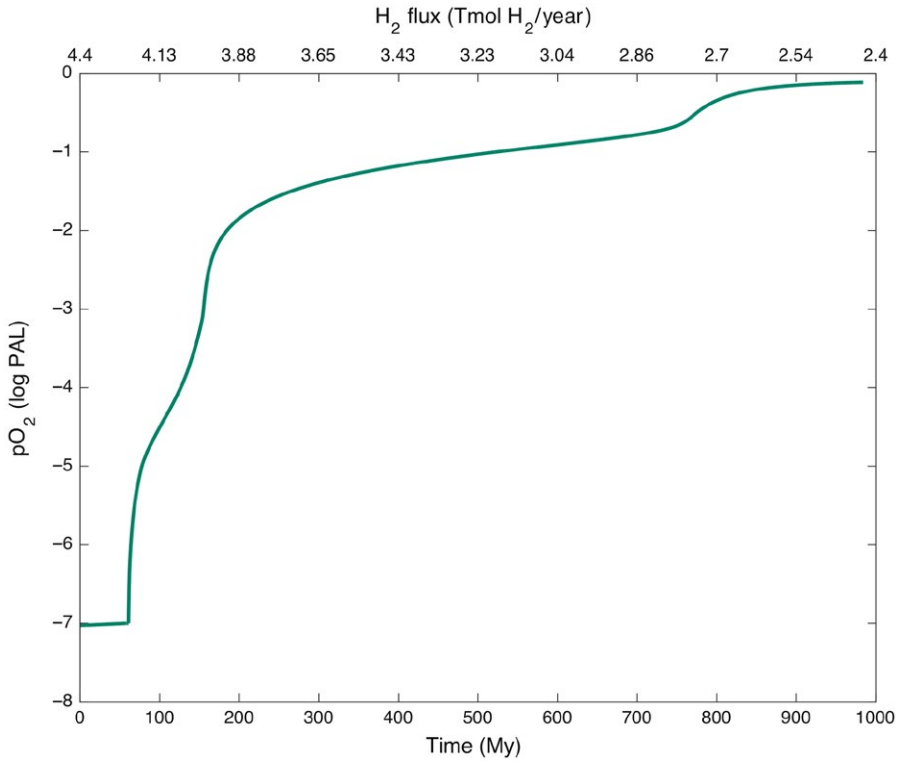

FIGURE 5 Evolution of atmospheric pO_2 from an Archean-like equilibrium state, assuming a secular decline in the outgassing of H_2 (see Section 2.4). pO_2 passes through periods with semi-stable values at Archean-, Proterozoic-, and Phanerozoic-like levels [Colour figure can be viewed at wileyonlinelibrary.com]

Archean level, and pO_2 eventually relaxes back to this steady state, for no net change in the atmosphere across the glacial event.

3.6 | Response of pO_2 to a secular decline in H_2 outgassing

The evolution of pO_2 from its low-oxygen state is shown in Figure 5, allowing for a secular decrease in the rate of hydrogen release from volcanoes and serpentinization. Oxygen levels vary extremely slowly until pO_2 reaches 10^{-7} PAL, the threshold for complete oxidation of subaerial pyrite. pO_2 then increases to 10^{-5} PAL in approximately 20 million years. Over the next 100 million years, pO_2 rises to 10^{-2} PAL. The final ascent to 10^{-1} PAL requires hundreds of millions of years. These timescales assume that the hydrogen flux declines with the square of mantle heat flow (Canfield, 2004; Turcotte, 1980). This rate of change can be compared to the simulations of Claire et al. (2006), which had similar results, although the actual rate of change, and even its sign, could be much more complex (see Section 2.2).

4 | DISCUSSION

4.1 | Stability of high oxygen, and the importance of phosphorus bioavailability

In the model, the modern oxygen budget is a balance between production of O_2 by organic carbon burial, and consumption of O_2 by net oxidation of the sulfur, iron, and hydrogen released through volcanism and weathering. The stability of this cycle arises from negative feedbacks associated with the oxidation and burial of organic carbon. Today, about 10% of the organic matter deposited on the seafloor is permanently buried, producing O_2; the remainder is re-oxidized in the sediment (Hedges & Keil, 1995). However, the efficiency of burial increases under low-oxygen conditions, due to a reduction in remineralization rates (Katsev & Crowe, 2015). A decrease in global oxygen levels increases organic carbon burial, driving pO_2 back toward its original value. The oxygen-sensitive kinetics of organic carbon weathering (Chang & Berner, 1999), iron oxidation (Millero, Sotolongo, & Izaguirre, 1987b), and sulfide oxidation (Millero, Hubinger, Fernandez, & Garnett, 1987a) are also forms of negative feedbacks. A decrease in oxygen levels slows down the consumption of O_2 by these processes, again driving pO_2 back toward its equilibrium value.

Stable pO_2 at less than 10% PAL is simulated in the model through a decrease in the supply of bioavailable phosphorus. If there were no inorganic sink for phosphorous, the flux of phosphorus to the ocean must always be balanced by the deposition of organic matter on the seafloor. Under Proterozoic oxygen conditions, we hypothesize that a substantial inorganic sink competes with phytoplankton for phosphorous, essentially lowering the bioavailability and stabilizing pO_2 at Proterozoic levels (Laakso & Schrag, 2014).

Phosphorus is primarily derived from apatite weathering. The kinetics of this process are not dependent on pO_2, but the fraction of the weathered P, which is available for biology may vary with oxygen concentrations. In modern environments, phosphate adsorbs to ferric oxides. The iron-bound pool, which is several times larger than the dissolved reservoir (Benitez-Nelson, 2000), is at least partially inaccessible to organisms. Low-oxygen conditions favor reduced forms of iron, which may be more efficient sinks for phosphate, including vivianite precipitation (Derry, 2015), scavenging by green rust, and

coprecipitation of phosphate-bearing ferric oxides (Laakso & Schrag, 2014). The exact relationship between pO_2 and the bioavailable fraction at a global level is difficult to constrain. In our model, we assume a positive relationship over a range of pO_2 levels (Methods). The bioavailable fraction plateaus at both very high and very low oxygen levels, representing thresholds at which ocean iron reservoirs are completely oxidized or reduced. Given the uncertainty in the relationship between bioavailability and pO_2, it is important to keep in mind that the absolute level of pO_2 depends on the parameterization of this relationship used in our simulations. We have used a single parameterization in our model. An alternate form would shift the steady-state pO_2 levels in all simulations, but the dynamical mechanisms for achieving multiple steady states are robust.

4.2 | Steady states of the surface redox cycle

The negative feedbacks associated with organic carbon burial and oxidation kinetics stabilize pO_2 at each of the steady-state values in Figure 1. However, multiple steady states are only possible if there are also positive feedbacks in the oxygen cycle. Two different feedbacks give rise to the three equilibrium states found in our model.

4.2.1 | Positive feedbacks

The first positive feedback arises from interactions between the iron, carbon, and phosphorus cycles. The kinetics of iron oxidation are linear in O_2 concentration (Millero et al., 1987b). Neglecting changes in sulfur cycling, delivery of ferrous iron concentrations will rise if oxygen levels decrease. Additional Fe^{2+} raises the ocean's alkalinity, which shifts carbon speciation toward carbonate ion. The saturation state of calcium carbonate increases, accelerating the global rate of $CaCO_3$ precipitation. Iron carbonates such as siderite, ankerite, and iron-substituted calcium carbonate will also precipitate more rapidly in a more alkaline, iron-rich environment. Our model only includes siderite precipitation, but the rate of formation for any iron carbonate phase is likely sensitivity to ferrous iron concentrations, and thus to oxygen levels. This relationship between oxygen levels and siderite precipitation was recently pointed out by Bachan and Kump (2015). At a given level of pCO_2, both mechanisms result in a larger carbon sink, forcing pCO_2 to decline. Falling pCO_2 cools the global temperature, slowing silicate weathering rates and the generation of alkalinity, until the carbon cycle returns to equilibrium (Walker et al., 1981).

A decrease in acidic weathering will affect also apatite dissolution, driving a decline in the bioavailable phosphorus flux, assuming no change in the bioavailability. This is a positive feedback: A decrease in oxygen results in a decrease in the oxygen source, by way of larger ferrous iron concentrations, faster carbonate precipitation, and slower rates of apatite weathering. If iron carbonates remove P from the bioavailable phosphate pool through adsorption, the feedback will be amplified, although we have not included this process here. The scaling of phosphate weathering with pO_2 is not linear. At sufficiently high levels of oxygen, the ferrous iron concentration becomes negligibly small in the total alkalinity budget, and this effect will only vary weakly with pO_2. However, the record of banded iron formations suggests ferrous iron concentrations were much higher in Archean and Paleoproterozoic oceans than they are today (Holland, 1984), and iron speciation data are consistent with ferrous-rich oceans through the Proterozoic (Poulton & Canfield, 2011) and possibly the Cambrian (Sperling et al., 2015).

An earlier model of biogeochemical cycling (Goldblatt et al., 2006) found two steady states, at approximately Archean and Proterozoic levels of atmospheric pO_2. These states arose from a positive feedback related to the impact of UV shielding by O_2 and O_3 on hydrogen oxidation rates. This effect is accounted for in our atmospheric chemistry parameterization, which is based on the same photochemical model (Pavlov & Kasting, 2002). We find this effect alone is too small to result in significantly different steady states, after accounting for a more complete set of negative feedbacks related to carbon, iron, and sulfur cycling.

The second positive feedback is the relationship between pO_2 and the bioavailability of phosphorus and pO_2. At a given weathering rate, lower levels of pO_2 result in a smaller flux of bioavailable phosphorus. Steady-state burial of organic matter can never exceed the supply of bioavailable phosphorus, so a decrease in pO_2 drives further decreases in the oxygen source. This effect is not linear. The positive feedback is strongest when the pO_2 is near 10% PAL (Methods). Far from this value, the relationship is weak, and negative feedbacks become more quantitatively important.

There is no direct evidence for a relationship between pO_2 and phosphorus bioavailability, although several mechanisms have been proposed, including vivianite precipitation (Derry, 2015) or ferrihydrite scavenging (Laakso & Schrag, 2014) in low-oxygen rivers. Including this effect in the model is not evidence that it exists; we have explicitly designed this relationship to yield multiple steady states. Rather, we argue that without such an effect, it is not possible to explain the difference between Proterozoic and Phanerozoic oxygen levels. The equilibrium value of pO_2 is strongly constrained by the availability of the limiting nutrient, phosphorus, which acts as the primary control on organic carbon burial and thus O_2 production (see Figure S1). Other changes to the Earth system, such as the hydrogen flux, can still drive large variations in the equilibrium oxygen level when the total oxygen reservoir is small, as in the Archean. However, once the total oxygen level is large, the relationship between P-supply, organic burial, and oxygen production leaves pO_2 relatively insensitive to most geochemical processes.

In the case of hydrogen outgassing, this insensitivity is demonstrated by Figure 1: Given a modern level of bioavailable phosphorus, Phanerozoic levels of pO_2 are stable even given a very large increase in H_2 supply. Similar results are found in a separate study exploring other major parameters in a related model (Laakso & Schrag, 2014). This suggests that other changes to the Earth system, which might have occurred between the Neoproterozoic and Paleozoic, such as variations in the hydrogen outgassing flux, in organic carbon burial efficiency, in phosphorus remobilization, or in respiration rates, cannot explain the observed change in oxygen levels. We therefore include a relationship between bioavailable phosphorus and pO_2 in order to explore an internally consistent model of Phanerozoic and Proterozoic pO_2 that is consistent with the geological record, and to

test how such a system would respond to large perturbations. This should be contrasted with the positive feedback that leads to separate Archean and Proterozoic states, which arises naturally from interactions between the iron, carbon, and phosphorus cycles included in our model.

4.2.2 | Anoxic Earth: the Archean

This state is characterized by pO_2 below 10^{-7} PAL, the threshold at which pyrite does not weather to completion in our model. The production of oxygen is too slow to oxidize both the volcanic hydrogen and continental pyrite exposed to the surface environment. The steady-state oxygen level is thus set by the kinetics of these oxidative processes, which are oxygen dependent. This provides the primary negative feedback that stabilizes the redox cycle.

Incomplete pyrite oxidation implies that some detrital grains are transported and buried in sedimentary settings without being oxidized. Detrital pyrite of this type is widely found before 2.4 Ga, but rarely in younger sediments (Holland, 1984). Consistent with this observation, our Archean state is defined by incomplete oxidation of subaerial pyrites. Stable, low levels of oxygen are achieved when the production of oxygen, as determined by phosphorus bioavailability, is too slow to oxidize both all the hydrogen and all the pyrite exposed at the surface, allowing the rapid kinetics of these reactions to set the equilibrium value of pO_2. The maximum oxygen level of the Archean state is therefore set by the choice of the threshold for complete pyrite oxidation, which is set to 10^{-7} PAL in our model. While this value is uncertain, it must be less than 10^{-5} PAL to be consistent with the mass-independent sulfur isotope record, and the resulting dynamics of the oxygen and sulfur cycles are consistent with the geological record of the Archean.

The mass of pyrite that is oxidized varies with the H_2 outgassing flux, which determines the equilibrium oxygen level of the model's low-oxygen state. For example, in the steady-state budget given in Table 1, ~90% of pyrite is oxidized. In this example, the H_2 flux was chosen to give oxygen levels close to the weathering threshold, where multiple equilibrium states can coexist. The Archean and Proterozoic stable states can coexist at a single H_2 outgassing rate because the siderite–phosphorus feedback allows additional oxygen production of ~0.8 Tmol O_2 y^{-1} when oxygen levels are high. The absence of detrital pyrite in post-Archean rocks requires the Proterozoic state to be above the pyrite weathering threshold. For the both Archean and Proterozoic states to coexist, this implies that at least 0.4 Tmol S y^{-1} pyrite may be oxidized in the Archean state, or 50% of the pyrite exposed at the surface today (Berner & Berner, 1996).

This fraction may have been lower if additional mechanisms further suppressed phosphorus bioavailability in the Archean, such as vivianite formation in a ferruginous ocean (Derry, 2015). For example, if bioavailability declines by an additional 30% between Proterozoic and Archean levels of oxygen (Figure S1), the resulting Archean steady state oxidizes only 25% of the pyrite exposed during weathering. This oxidized fraction can be arbitrarily low in our modeled Archean state if one does not require both the Archean and Proterozoic states to coexist at single hydrogen outgassing rate. At sufficiently large H_2 flux, Archean pO_2 can fall to levels well below the weathering threshold (Figure 1), and a smaller fraction of pyrite would have been oxidized.

Detrital grains typically do not show signs of extensive surface oxidation, suggesting that physical abrasion was the primary mode of weathering in the Archean environment (Johnson et al., 2014). Quartz-dominated sediment transport in modern rivers has more than half its mass in particles with diameters less than 100 micrometers; in some rivers, this threshold is closer to 10 micrometers, or even less (Walling & Moorehead, 1989). Pyrite grains would likely be even smaller due to their lower Mohs hardness (Kowalewski & Rimstidt, 2003). At oxygen levels of 10^{-7} PAL, oxidation can reduce the radius of pyrite grains by tens to hundreds of micrometers in a typical river system (Johnson et al., 2014), suggesting that oxidation could have consumed the majority of surface pyrite while preserving the largest detrital grains.

In the low-oxygen state, the dominant redox-sensitive species in the water column in the model are ferrous iron and sulfide. It is difficult to predict the equilibrium levels exactly given the complex kinetics of pyrite and siderite formation (Rickard & Luther, 2007); our model stabilizes with micromolar levels of iron and sulfide, with iron dominating. A ferruginous ocean is consistent with the record of banded iron formation in the Archean, which is thought to have required transport of large quantities of dissolved iron without titration by oxygen or sulfide (Holland, 1984). Sulfate is 0.7 mM. This is of the same order as 1 mM value proposed by Shen, Canfield, and Knoll (2002) for the Proterozoic oceans.

The Archean-like atmosphere in our model has hydrogen concentrations of 0.1 ppm, on the order of modern levels, suppressed by rapid oxidation kinetics even at low levels of O_2. The corresponding rate of escape is 0.5 Gmol H_2 y^{-1}, or approximately $2*10^6$ cm^{-2}/s. The depleted D/H ratio in 3.8 Ga serpentines has been used to estimate total hydrogen loss of 10^{22} mol H_2 over Earth history (Pope, Bird, & Rosing, 2012). For this to have occurred, the bulk of the escape must have taken place before the evolution of oxygenic photosynthesis, when very low oxygen levels would have permitted much larger hydrogen concentrations and rates of escape.

Methane concentrations in this atmosphere are on the order of one ppb, suggesting that methane did not play a substantial role in warming the Archean Earth. These low levels are the result of a low rate of biological methanogenesis. Methanogens are responsible for about half of all organic carbon consumption, approximately 10% of primary production, but this generates only 0.1 Tmol CH_4 y^{-1}. Earlier models of Archean redox cycling assumed that, in the absence of oxygen, methanogenesis alone can maintain much higher rates of organic carbon degradation, possibly similar to those observed in the modern ocean or the Black Sea (Pavlov, Brown, & Kasting, 2001). However, isotopic mass balance in Lake Matano, Indonesia, indicates that only about 10% of the organic matter exported into its ferruginous deep waters is degraded via methanogenesis, consistent with our model. This flux may have been larger if the Archean were host to a substantial terrestrial biosphere that could survive the absence of a UV-shielding ozone layer (Lalonde & Konhauser, 2015).

Abiotic methane production in serpentinizing systems is another possible source of methane. Observations of modern vent systems constrain this 10% of total hydrogen production (Keir, 2010), or

0.2 Tmol CH_4 y^{-1}, the value used here. The combined biotic and abiotic methane source is balanced by photo-oxidation at the part-per-billion atmospheric concentrations. If oxygen levels were substantially lower than 10^{-7}, either earlier in the Archean (or in the Hadean), methane mixing ratios may have been as high as 10^{-5}.

This Archean-like state requires the total source of oxygen to be smaller than the oxygen sink represented by hydrogen outgassing and pyrite exposure. The oxygen source is small in this state because the bioavailability of phosphorus is only a third of the present-day rate. This is due to two effects. First, the bioavailability of phosphorus is only a third of it modern value in a low-oxygen environment due to phosphorous scavenging by iron minerals, as discussed above. Second, a ferruginous ocean precipitates iron carbonate minerals, suppressing CO_2 and slowing the rate of apatite weathering. Inefficient remineralization of organic P results in subnanomolar P concentrations in the deep ocean. Phosphate-poor upwelling starves the surface of nutrients, supporting only 0.1% of modern primary production. Although export and burial of NPP are over 90% efficient, the net oxygen source is still less than 70% of its modern value. Oxidation of H_2 and of continental pyrite, both of which have rapid kinetics even at low oxygen levels, are sufficient to balance this small source at a very low equilibrium level of pO_2. A reduced supply of bioavailable phosphorus, leading to limited organic carbon burial, is the mechanism by which the atmosphere is stabilized at Archean levels of pO_2 in the presence of oxygenic photosynthesis.

There is no undisputed biomarker evidence for oxygenic photosynthesis in the Archean (Rasmussen, Fletcher, Brocks, & Kilburn, 2008), and it has been suggested that the rise to Proterozoic oxygen levels was the immediate result of the evolution of this metabolic process at 2.4 Ga (Kopp et al., 2005). However, several lines of evidence are consistent with the existence of oxygenic photosynthesis hundreds of millions of years before the Archean–Proterozoic boundary, including local molybdenum enrichment (Lyons Reinhard & Planavsky, 2014) and the structure of stromatolites (Bosak et al., 2013). Equilibration of our model at 10^{-7} PAL demonstrates that Archean levels of pO_2 are sustainable in the presence of oxygenic photosynthesis, and implies that the oxygenation of the Earth's surface would not have happened without a sufficient perturbation to overwhelm the negative feedbacks that stabilize pO_2 at these levels.

4.2.3 | Low-oxygen Earth: the Proterozoic

The intermediate-oxygen state is characterized by pO_2 between 10^{-3} and 10^{-1} PAL. At this level of oxygen, pyrite weathering proceeds to completion. The range of oxygen levels and the complete weathering of pyrite are consistent with the proxy record of the Proterozoic (Johnson et al., 2014; Planavsky et al., 2014). Pyrite oxidation occurs at its maximum rate, and so does not vary with pO_2 and cannot provide negative feedback. Stabilization arises from the oxygen-sensitive kinetics of iron and sulfide oxidation in the water column; given a transient increase in pO_2, a greater proportion of iron and sulfur are oxidized and buried, drawing oxygen back down to its equilibrium level. Additional negative feedback is provided by oxygen-sensitive burial efficiency of organic carbon. A rise in oxygen levels results in more extensive oxic respiration in the sediment (Hedges et al., 1999), releasing P to the pore waters where it may precipitate in authigenic forms. This allows closure of the P budget with less organic carbon burial, driving oxygen back toward equilibrium.

The bioavailability of phosphorus is essentially the same in this state and the low-oxygen state, roughly one-third of modern. However, the total flux of phosphorus into the ocean is higher due to an increase in the overall weathering rate, driven by the increase in pCO_2 required to compensate for the loss of siderite precipitation in the more oxidized ocean, via the oxygen–alkalinity feedback described above. This leads to an increase in the source of oxygen via organic carbon burial, which is balanced by an equivalent increase in iron oxidation rates, leading to a new steady-state balance.

The relative increase in pO_2 from the Archean to the Proterozoic state is 300 times larger than the relative change in organic burial rate. This difference in scale is due to a nonlinearity in the pyrite weathering rate as a function of oxygen. In the Archean state, the oxygen source is not large enough to oxidize both all the hydrogen and all the sulfide being exposed to the surface environment. In the Proterozoic state, the oxygen source is larger than this combined sink, and excess O_2 production must accumulate in the atmosphere until the kinetics of iron oxidation become fast enough to close the oxygen budget. The equilibrium oxygen level is set by balancing organic carbon burial against pyrite weathering kinetics in the Archean case, and by iron oxidation kinetics in the Proterozoic, so there is no reason to expect a smooth linear scaling between organic carbon burial and pO_2.

The equilibrium level of oxygen is sensitive to the effective global oxidation rate constants. The tuning used here allows for equilibrium at values ranging from 0.5% PAL to 10%. This is consistent with a range of earlier estimates (Canfield & Teske, 1996; Holland, 1984), and slightly higher than the more recent estimates based on chromium isotopes (Planavsky et al., 2014). Varying the effective rate constants would allow for equilibrium at different values of pO_2. More importantly, our results demonstrate that positive feedbacks arising from the joint cycles of iron, carbon, and phosphorus can give rise to stable oxygen levels that are widely separated and order of magnitude consistent with the proxy record.

Although oxygen levels are much higher in the Proterozoic state, the carbon cycle is similar to the Archean. Remineralization rates remain slow, and organic carbon burial efficiency high. Without significant nutrient remineralization, the 7% increase in apatite weathering only leads to 7% increases in NPP and organic carbon burial relative to the Archean. Primary production is 4 Tmol C y^{-1}, approximately 0.1% of the modern value. As in the Archean, very low levels of primary productivity are required to maintain a low rate of oxygen production, given that production is buried with more than 70% efficiency. Our model assumes production is phosphorus-limited, and therefore, the reduction in productivity is driven by a drop in the bioavailability of phosphorus. Others have argued for limitation by nitrogen during the Proterozoic, due either to changes in the relative rates of nitrification and denitrification in the low-oxygen environment (Fennel, Follows, & Falkowski, 2005), or to trace metal stress on diazotrophs (Planavsky

et al., 2010). Given the low rates of primary production required to stabilize the oxygen budget, the biological demand for fixed nitrogen is no more than 0.1% of its modern value throughout the Precambrian. This is equivalent to 0.6 Tmol N y^{-1} in our model, assuming average biomass of 106C:16N. Today, lightning strikes alone fix 0.4 Tmol N y^{-1} (Galloway et al., 2004), suggesting that limitation by nitrogen, either directly or through trace metal stress, is unlikely.

Sulfide, ferrous iron, and oxygen concentrations in the ocean are relatively close to each other in this environment: 0.002, 0.03, and 0.5 μM, respectively (Table 1). Though oxygen dominates average ocean water in this case, local variations, such as in oxygen minimum zones or near hydrothermal systems, could push local conditions to sulfidic or ferruginous. These local variations are consistent with iron speciation studies that suggest zones of oxic, sulfidic, and ferruginous conditions existed along depth profiles in Proterozoic basins (Poulton, Fralick, & Canfield, 2010). The sulfate concentration is 0.9 mM, consistent with predictions of approximately 1 mM derived from the observed variability in the $\delta^{34}S$ of Proterozoic sulfides (e.g., Shen et al., 2002).

An important geological constraint on Precambrian carbon and oxygen cycling is that the $\delta^{13}C$ of sedimentary carbonates has remained close to 0‰ over much of geologic time (Prokoph, Shields, & Veizer, 2008). Using a simple model of carbon mass balance, this observation can be used to derive f_{org}, the organic fraction of total carbon burial:

$$(\delta^{13}C)_{volc.} = ((\delta^{13}C)_{CaCO_3} - \varepsilon)f_{org} + (\delta^{13}C)_{CaCO_3}(1 - .f_{org}) \quad (5)$$

where ε is fractionation due to RuBisCo, and the isotopic composition of calcium carbonate is assumed to reflect the composition of seawater. This mass balance implies that organic carbon burial should account for about 20% of net carbon burial over most of Earth history; our modern model gives a value of 29%. Both the Proterozoic and Archean states are characterized by larger fractions, 46% and 37%, respectively. Note that the *net* organic fraction is larger than its modern value, despite the absolute decrease in organic carbon burial, due to the complete lack of organic carbon weathering.

This apparent incongruity may be explained by systematic differences in the formation of authigenic carbonates over time. Authigenic carbonates are often found in low-oxygen sedimentary environments, where sulfate and iron reduction produces alkalinity that can result in supersaturation of calcium carbonate in the pore waters. The pool of dissolved carb in these environments may be depleted relative to seawater, due to oxidation of organic material, or enriched relative to seawater, due to methanogenesis (Schrag et al., 2013). In order to produce marine carbonates with a $\delta^{13}C$ value near 0‰ despite an increase in f_{org}, one would expect additional formation of isotopically enriched authigenic carbonate in the Proterozoic and Archean. Though we cannot explicitly simulate pore-water processes in our simple ocean model, this is consistent with our results, which feature a four- to fivefold increase in methanogenesis in the Precambrian compared with our modern simulation.

A high value of f_{org}, coupled with a constant volcanic input of volcanic carbon, implies that the Proterozoic carbon cycle was a larger net source of oxygen than it is today. However, this is offset by a corresponding decrease in the fraction of sulfur being removed as pyrite, f_{pyr}, which is approximately 10% in our model, compared with the 40% estimated for the modern biogeochemical cycle. This is associated with the relatively small flux of organic carbon to the sediment, which supports limited sulfide production. A low value of f_{pyr} conflicts with the conventional reading of the $\delta^{34}S$ record, which suggests that approximately pyrite is the primary sulfur sink throughout the Precambrian (Canfield 2004). This interpretation relies on several assumptions, including a constant value for isotopic input of sulfur from weathering, and sparse $\delta^{34}S$ sulfate measurements in the Mesoproterozoic.

However, high f_{org} and low f_{pyr} are not fundamental aspects of biogeochemical cycling in a low-oxygen world. It is possible that, even in the absence of large organic carbon loading, sulfate reduction rates are much higher in a low-oxygen environment, due to the increased lability of the organic carbon reaching the sediment column (Westrich & Berner, 1984). If this effect is included in the model, it is possible to produce a stable, low-oxygen simulation with f_{org} values closer to the modern baseline, and f_{pyr} values of approximately 75%. We have chosen to present simulations with large values of f_{org} to highlight the challenges in interpreting the $\delta^{13}C$ and $\delta^{34}S$ records as O_2 proxies. However, both versions of the model can be tuned to reproduce modern geochemical cycling, while also allowing for three simultaneously stable levels of pO_2. The robust result is that steady-state pO_2 of less than 10% PAL requires a smaller supply of bioavailable phosphorus to the ocean. This results in less net burial of reductant, and thus less oxygen production. The reductant in question may have been either organic carbon or primarily pyrite; both are consistent with low pO_2, but make different predictions for the records of $\delta^{13}C$ and $\delta^{34}S$.

4.2.4 | High-oxygen Earth: the Phanerozoic

The high-oxygen state is characterized by oxygen levels greater than 40% PAL, which is also the lower bound on the oxygen content of the post-Devonian atmosphere (Kump, 2008). At this level of oxygen, the bioavailability of phosphorus increases toward modern levels. This permits a much larger rate of organic carbon burial than in the Archean or the Proterozoic, even as the burial efficiency of primary production falls to less than 1%. At this high level of pO_2, more rapid oxidative weathering of organic carbon burial, and the decreasing efficiency of organic carbon burial all bring the oxygen budget back to equilibrium. The negative feedbacks that applied in the Proterozoic remain relevant, and the oxygen sensitivity of organic carbon weathering (Chang & Berner, 1999) provides additional stability.

We note that our simple model lacks some important components of modern redox cycles, including a terrestrial carbon cycle. Inclusion of terrestrial carbon (and sulfur) cycling may be important in explaining variability within the Phanerozoic. Recent work on iron speciation (Sperling et al., 2015) is more consistent with a series of smaller changes in pO_2 across the Paleozoic. The Proterozoic/Phanerozoic transition described here could simply be the first of these changes, with subsequent increases in oxygen driven by an accumulation of smaller changes, such as changes in phosphorus weathering related to the evolution of land plants, or changes in sedimentary phosphorus regeneration associated with the evolution of bioturbation.

4.3 | Steady-state pO_2 and the oxidation events

During both the Great Oxidation Event and the Neoproterozoic oxidation event, atmospheric pO_2 rose by orders of magnitude over a relatively short period of time, and then maintained a more oxidized condition for hundreds of millions of years afterward. Many existing models for this transition focus on changes in redox dynamics driven by external events, such as the development of new metabolic processes (Kopp et al., 2005) or waste packaging methods (Butterfield, 2009; Logan et al., 1995), stabilization of continental cratons (Kump & Barley, 2007), or long-term oxidation of the Earth due to hydrogen escape (Catling et al., 2001). The identification of multiple steady states for pO_2 in our model implies that a large change in pO_2 is possible without any change in the redox dynamics themselves. Instead, the change can be triggered by a transient perturbation that drives Earth's surface from one steady state to another. We can use our model to place basic constraints on the scale and type of perturbation required to explain each of the two oxidation events.

The transition from Archean to Proterozoic depends on the cessation of siderite production under high oxygen levels. Without this sink for carbon, pCO_2 must rise until calcium carbonate precipitation becomes rapid enough to compensate. The associated increase in apatite weathering then leads to additional oxygen production, stabilizing O_2 at a higher value. Of the chemical species involved in this mechanism, calcium has the longest lifetime in the modern ocean. Following a perturbation to O_2, CO_2, or Fe^{2+}, the pulse in atmospheric oxygen will decay due to negative feedbacks in less time than is required for calcium concentrations to relax to their Proterozoic values. Therefore, the perturbation most likely to result in a transition between the Archean and Proterozoic steady states is one that impacts not only oxygen, but also the calcium budget. The transition between the Proterozoic and Phanerozoic states depends on a positive feedback between pO_2 and the bioavailability of phosphate. This feedback depends only on changes in the oxygen budget, and therefore a perturbation only in O_2 would be sufficient to drive a transition from Proterozoic to Phanerozoic levels of O_2.

4.4 | Snowball Earth as a redox perturbation

A Snowball Earth glaciation is a compelling candidate to provide a redox perturbation sufficient to shift the atmosphere from one steady state to another because Snowball glaciations coincide with both major oxidation events (Hoffman & Schrag, 2002). The second of two Paleoproterozoic glaciations has been correlated with the Great Oxidation Event (Hoffman, 2013); all oxidized facies appear to fall above the second glaciation, and all reduced units below. Similarly, the Marinoan glaciation, the second of the Neoproterozoic Snowball events, has been linked with an increase in the oxidation state both through changes in trace metal abundances across the glaciation (Sahoo et al., 2012), and based on the first appearance of fossils of large, multicellular animals soon after the glaciation (Hoffman & Schrag, 2002).

Our model results provide a deeper understanding for the mechanisms through which a Snowball glaciation may perturb the redox cycles, allowing the Earth to transition from one stable state to another. In a Snowball glaciation, there is both a transient increase in atmospheric CO_2 and a decrease in alkalinity generation, due to a slowdown in weathering rates associated with ice cover and low temperatures (Hoffman et al., 1998). There is also a significant pulse of atmospheric O_2, driven by two mechanisms described below, one of which operates during the glacial period and one in the post-glacial period.

During a Snowball glaciation, primary production continues in cracks, polynyas, or larger open areas in the ice sustained by local geothermal sources of heat. The majority of this local oxygen production is released to the atmosphere due to the low solubility of O_2, with the remainder advected into the unproductive waters under the ice. Although the ocean becomes increasing reduced, atmospheric oxygen levels increase as the extensive ice cover decouples the atmosphere from its sinks in the oceans and on the continents, essentially short-circuiting the negative feedbacks (burial of organic carbon and oxidation of reduced species in seawater) that help to stabilize pO_2. Thus, as long as nutrient input during the glaciation is sufficient to sustain some low level of productivity, oxygenation of the atmosphere will proceed during a Snowball glaciation. One possible source of sustained nutrient input is subglacial weathering, and discharge to seawater.

A second mechanism for producing a transient increase in oxygen during a Snowball glaciation is the period of rapid weathering, which follows the melting of a Snowball. Very high levels of CO_2 result in elevated weathering rates, which increase the flux of phosphorus to the oceans, driving additional organic matter burial and a pulse of oxygen production. This post-glacial oxygen production depends on the intensity of weathering, controlled by peak pCO_2 levels, while intraglacial oxygen production depends on the duration of the glacial episode. Both factors must be known to predict the trajectory of pO_2 during and after an event. Since these values are poorly known for Earth's Snowball events, it is difficult to determine whether a particular glacial would have driven a transient or permanent change in pO_2. Nevertheless, our simulations show that a combination of these two mechanisms can produce enough oxygen to drive the ocean and atmosphere into the stability regime of a more oxidized steady state (Figure 4).

An alternative hypothesis for the GOE that the oxidation state of the mantle or of volcanic gases increased during the late Archean (Kasting, 1993). The vanadium content of basalts, however, suggests the oxidation state has been stable since at least 3.0 Ga (Li & Lee, 2004). Kump and Barley (2007) have argued for a change to the oxidation state of volcanic fluids themselves, driven by a shift in the equilibration pressure and temperature following the switch from predominantly submarine to subaerial volcanism after the stabilization of continental cratons in the late Archean. Others have asserted a slow decline in the hydrogen outgassing rate as the mantle cools, which has been shown to produce oxidation of the atmosphere in an earlier model (Claire et al., 2006). The kinetics associated with oxidation of the crust may also have slowed as the bulk continents are oxidized due to ongoing oxygen production via photolysis of water followed by hydrogen escape (Catling et al., 2001).

Any of these hypotheses can be represented in our model by a decline in the hydrogen flux over time. For an H_2 flux below 4.3 Tmol H_2 y^{-1}, the Archean state ceases to be stable, and oxygen must rise to its Proterozoic value (Figure 5 see also Claire et al., 2006). In this particular

simulation, Proterozoic levels of oxygen persist for only 1 billion years, but this could be altered by assuming a different rate of change in the outgassing rate. These explanations for the GOE are thus consistent with the dynamics of our model. A challenge to this model of oxidation is that it does not obviously explain the simultaneity of the Snowball events and oxidation. Some others (e.g., Kopp et al., 2005) have argued that oxidation induces global glaciation via a collapse in methane. As we have argued here, methane levels were unlikely to have been very high in the late Archean, making this scenario unlikely. Furthermore, this hypothesis does not appear to be consistent with the geological evidence suggesting the GOE occurred across the second Paleoproterozoic Snowball rather than the first (Hoffman, 2013). A glacial trigger for the Great Oxidation Event resolves this problem by providing a mechanism for linking oxidation and glaciation in some cases but not others.

This hypothesis depends on a significant role for iron carbonates in the Archean carbon cycle. Our simple model relates the rate of iron carbonate formation to ferrous iron concentrations and carbonate speciation, but does not account for competition with other potentially important phases, such as iron silicates. However, the hypothesis makes testable predictions for the geologic record. Our simulations predict a large difference in sedimentary iron phases before and after the Great Oxidation Event. Iron carbonates, represented in our model as siderite but possibly including ankerite or iron-substituted calcium carbonate, should be much more prevalent in sediments older than 2.4 Ga, although vulnerability to oxidation during metamorphism may limit their preservation. The rise in oxygen, in addition to preventing precipitation of new siderite, may have resulted in a major alteration event, in which Archean siderite exposed to Proterozoic surface conditions was oxidized (Bachan & Kump, 2015). Banded iron formations (BIFs) have an average iron oxidation state of +2.4, and commonly contain a major siderite and ankerite component (Klein & Beukes, 1993). BIF deposition has a volumetric peak around 2.5 Ga (Klein, 2005), with only sporadic formation after the Paleoproterozoic. Iron carbonates can be found in both Proterozoic (Planavsky et al., 2011; Poulton et al., 2010) and Archean (Kendall et al., 2010; Raiswell et al., 2011) shales, but they represent a smaller fraction of the total iron pool in the Proterozoic sections. A compilation of measurements on carbonates (Veizer, 1978) shows a continuous increase in the iron content back through time, with the change dominated by ferrous iron. This is consistent with our prediction, though the data do not show a step function in the Paleoproterozoic. The ferrous iron may not be present as primary siderite, but may have substituted into the carbonate lattice during early diagenesis (Veizer, 1978). Though mechanistically different than our model of primary siderite, iron carbonate formation during early diagenesis should yield similar dynamical behavior, as long as the rate of formation is dependent on iron concentration in the oceans.

Our glacial mechanism for the GOE implies that oxygen must also have risen, at least transiently, following the Cryogenian glacial events. This is consistent with extensive deposition of iron oxides following the Sturtian (Hoffman & Schrag, 2002). Titration of a large marine iron reservoir may have suppressed pO_2 back to low levels between glacials (see Figure 4). Oxidation of the ocean at the expense of the atmosphere would have primed Earth's surface for a larger increase in pO_2 during the Marinoan glaciation. The Marinoan rise in oxygen appears to have led to a permanent transition into a high-oxygen, Phanerozoic state, consistent with post-Marinoan changes in trace metal abundances and isotopes (Sahoo et al., 2012, Reinhard et al., 2013; Partin et al., 2013), along with large-scale deposition of barites (Hoffman & Schrag, 2002) and the expansion in large-bodied organisms (Anbar & Knoll, 2002).

Steady-state pO_2 in the Paleozoic may still have been below modern levels. The evolution of land plants during the Devonian created a source of organic matter with a large C:P ratio, allowing for more organic carbon burial without a change in phosphorus supply. This may have driven an additional increase in pO_2, from Paleozoic to modern levels (Lenton et al., 2016). Given that different redox proxies may be sensitive to different oxygen thresholds (Lyons Reinhard & Planavsky, 2014), this model can explain why trace metals record rising pO_2 in the early Ediacaran, while iron speciation data indicate oxygenation in the Devonian (Sperling et al., 2015).

If the hypothesized connection between glaciation and oxygenation is correct, an important implication is that modern levels of atmospheric oxygen were not inevitable. Some have understood the redox history of the Earth surface to be a slow, unstoppable march toward higher oxidation state, driven by burial of organic carbon following the evolution of photosynthesis. Our finding is in sharp contrast with this framing. If the Snowball glaciations near the Archean–Proterozoic and Proterozoic–Phanerozoic boundaries had not occurred (or perturbations of equivalent magnitude), then our model implies that oxygen levels would have remained at Archean or at Proterozoic levels until such a perturbation occurred, barring a sufficiently large decline in hydrogen outgassing rates. The total inventory of oxidized iron and sulfur does accumulate through time as the pool of sedimentary organic carbon grows (e.g., Hayes & Waldbauer, 2006), but these inventories are decoupled from the steady-state concentration of atmospheric O_2. In this context, the Snowball glaciations play an even more fundamental role in Earth history than previously imagined, driving the transitions from one redox state to another.

5 | CONCLUSIONS

Using a simple, mechanistic model of the biogeochemical cycles of redox-sensitive species, we show that redox dynamics in Earth's ocean and atmosphere result in multiple steady levels of atmospheric O_2. The pO_2 values and redox cycling of these states are consistent with the geological records of the Archean, Proterozoic, and Phanerozoic, respectively. In this context, both the GOE and the Neoproterozoic oxidation event can be explained as a jump between stable states, driven by transient perturbations to pO_2; our model suggests that the GOE may also be sensitive to perturbations in pCO_2 and alkalinity. We show that Snowball glaciations can drive a jump in pO_2 through two separate mechanisms and also affect the carbon and alkalinity cycle in a manner required in our model to transition from one stable state to another. If our mechanistic explanation is correct, it implies that these environmental perturbations were more than just "bottlenecks" for the evolution of life, but actually drove the environmental transitions, uncorking the bottle and allowing biological evolution to respond.

ACKNOWLEDGMENTS

We thank Dimitar Sasselov for many helpful discussions and for assistance with hydrogen escape calculations. We thank Lee Kump, Dave Johnston, Andy Knoll, and Paul Hoffman for suggestions. This work was supported by Henry and Wendy Breck and the Simons Foundation. Portions of this work were supported by NASA Headquarters under the NASA Earth and Space Science Fellowship Program Grant NNX11AP89H.

REFERENCES

Abbott, D., & Hoffman, S. (1984). Plate tectonics revisited 1. Heat flow, spreading rate, and the age of subducting oceanic lithosphere and their effects on the origin and evolution of continents. *Tectonics*, *3*, 429–448.

Anbar, A., Duan, Y., Lyons, T., Arnold, G., Kendall, B., Creaser, R., Kaufman, A., Gordon, G., Scott, C., Garvin, J., & Buick, R. (2007). A whiff of oxygen before the great oxidation event? *Science*, *317*, 1903–1906.

Anbar, A., & Knoll, A. (2002). Proterozoic ocean chemistry and evolution: a bioinorganic bridge? *Science*, *297*, 1137–1142.

Bachan, A., & Kump, L. (2015). The rise of oxygen and siderite oxidation during the Lomagundi Event. *Proceedings of the National Academy of Sciences of the United States of America*, *112*, 6562–6567.

Benitez-Nelson, C. (2000). The biogeochemical cycling of phosphorus in marine systems. *Earth Science Reviews*, *51*, 109–135.

Bergman, N., Lenton, T., & Watson, A. (2004). COPSE: a new model of biogeochemical cycling over Phanerozoic time. *American Journal of Science*, *304*, 397–437.

Berner, E., & Berner, R. (1996). *Global environment: water, air, and geochemical cycles*. Upper Saddle River NJ: Prentice Hall.

Bosak, T., Knoll, A., & Petroff, A. (2013). The meaning of stromatolites. *Annual Review of Earth & Planetary Sciences*, *41*, 21–44.

Butterfield, N. (2009). Oxygen, animals and oceanic ventilation: an alternative view. *Geobiology*, *7*, 1–7.

Canfield, D. (2004). The evolution of the Earth surface sulfur reservoir. *American Journal of Science*, *304*, 839–861.

Canfield, D., Rosing, M., & Bjerrum, C. (2006). Early anaerobic metabolisms. *Philosophical Transactions of the Royal Society B: Biological Sciences*, *361*, 1819–1836.

Canfield, D., & Teske, A. (1996). Late Proterozoic rise in atmospheric oxygen concentration inferred from phylogenetic and sulphur-isotopes studies. *Nature*, *382*, 127–132.

Cannat, M. (1993). Emplacement of mantle rocks in the seafloor at mid-ocean ridges. *Journal of Geophysical Research*, *98*, 4163–4172.

Catling, D., Zahnle, K., & McKay, C. (2001). Biogenic methane, hydrogen escape, and the irreversible oxidation of the early Earth. *Science*, *293*, 839–843.

Chang, S., & Berner, R. (1999). Coal weathering and the geochemical carbon cycle. *Geochimica Cosmochimica Acta*, *63*, 3301–3310.

Claire, M., Catling, D., & Zahnle, K. (2006). Biogeochemical modelling of the rise in atmospheric oxygen. *Geobiology*, *4*, 239–269.

Colman, A., & Holland, H. (2000). The global diagenetic flux of phosphorus from marine sediments to the oceans: redox sensitivity and the control of atmospheric oxygen levels. In C. Glenn, L. Prévôt-Lucas, & J. Lucas (Eds.), *Marine authigenesis: from global to microbial* (pp. 53–75). Tulsa: Society for Sedimentary Geology.

Derry, L. (2015). Causes and consequences of mid-Proterozoic anoxia. *Geophysical Research Letters*, *42*, 8538–8546.

Farquhar, J., Zerkle, A., & Bekker, A. (2011). Geological constraints on the origin of oxygenic photosynthesis. *Photosynthesis Research*, *107*, 11–36.

Fennel, K., Follows, M., & Falkowski, P. (2005). The co-evolution of the nitrogen, carbon and oxygen cycles in the Proterozoic ocean. *American Journal of Science*, *305*, 526–545.

Forster, P., Ramaswamy, V., Artaxo, P., Berntsen, T., Betts, R., Fahey, D., Haywood, J., Lean, J., Lowe, D., Myhre, G., Nganga, J., Prinn, R., Raga, G., Schulz, M., & Van Dorland, R. (2007). Changes in atmospheric constituents and in radiative forcing. In S. Solomon, D. Qin, M. Manning, Z. Chen, M. Marquis, K. Averyt, M. Tignor & H. Miller (Eds.), *Climate change 2007: the physical science basis. Contribution of working group I to the fourth assessment report of the intergovernmental panel on climate change* (pp. 129–234). Cambridge University Press, New York.

Galloway, J., Dentener, F., Capone, D., Boyer, E., Howarth, R., Seitzinger, S., Asner, G., Cleveland, C., Green, P., Holland, E., Karl, D., Michaels, A., Porter, J., Townsend, A., & Vörösmarty, C. (2004). Nitrogen cycles: past, present, and future. *Biogeochemistry*, *70*, 153–226.

Goldblatt, C., Lenton, T., & Watson, A. (2006). Bistability of atmospheric oxygen and the Great Oxidation. *Nature*, *443*, 683–686.

Gough, D. (1981). Solar interior structure and luminosity variations. *Solar Physics*, *74*, 21–34.

Grotzinger, J., & Kasting, J. (1993). New constraints on precambrian ocean composition. *Journal of Geology*, *101*, 235–243.

Habicht, K., Gade, M., Thamdrup, B., Berg, P., & Canfield, D. (2002). Calibration of sulfate levels in the Archean Ocean. *Science*, *298*, 2372–2374.

Hayes, J., & Waldbauer, J. (2006). The carbon cycle and associated redox processes through time. *Philosophical Transactions of the Royal Society B: Biological Sciences.*, *361*, 931–950.

Hedges, J., Hu, F. S., Devol, A., Hartnett, H., Tsamakis, E., & Keil, R. (1999). Sedimentary organic matter preservation: a test for selective degradation under oxic conditions. *American Journal of Science*, *299*, 529–555.

Hedges, J., & Keil, R. (1995). Sedimentary organic matter preservation: an assessment and speculative synthesis. *Marine Chemistry*, *49*, 81–115.

Hoffman, P. (2013). The great oxidation and a siderian snowball Earth: MIF-S based correlation of Paleoproterozoic glacial epochs. *Chemical Geology*, *362*, 143–156.

Hoffman, P., Kaufman, A., Halverson, G., & Schrag, D. (1998). A neoproterozoic snowball earth. *Science*, *281*, 1342–1346.

Hoffman, P., & Schrag, D. (2002). The snowball Earth hypothesis: testing the limits of global change. *Terra Nova*, *14*, 129–155.

Holland, H. (1984). *The chemical evolution of the atmosphere and oceans*. Princeton: Princeton University Press.

Holland, H. (2002). Volcanic gases, black smokers, and the great oxidation event. *Geochimica Cosmochimica Acta*, *66*, 3811–3826.

Hunten, D. (1973). The escape of light gases from planetary atmospheres. *Journal of Atmospheric Sciences*, *30*, 1481–1494.

Isley, A., & Abbott, D. (1999). Plume-related mafic volcanism and the deposition of banded iron formation. *Journal of Geophysical Research*, *104*, 15461–15477.

Johnson, J., Gerpheide, A., Lamb, M., & Fischer, W. (2014). O_2 constraints from Paleoproterozoic detrital pyrite and uraninite. *Geological Society of America Bulletin*, *126*, 813–830.

Kasting, J. (1993). Earth's Early atmosphere. *Science*, *259*, 920–926.

Katsev, S., & Crowe, S. (2015). Organic carbon burial efficiencies in sediments: the power law of mineralization revisited. *Geology*, *43*, 607–610.

Keir, R. (2010). A note on the fluxes of abiogenic methane and hydrogen from mid-ocean ridges. *Geophysical Research Letters*, *37*, 1–5.

Kendall, B., Reinhard, C., Lyons, T., Kaufman, A., Poulton, S., & Anbar, A. (2010). Pervasive oxygenation along late Archaean ocean margins. *Nature Geoscience*, *3*, 647–652.

Kennedy, M., Droser, M., Mayer, L., Pevear, D., & Mrofka, D. (2006). Late precambrian oxygenation; inception of the clay mineral factor. *Science*, *311*, 1446–1449.

Klein, C. (2005). Some Precambrian banded iron-formations (BIFs) from around the world: Their age, geologic setting, mineralogy, metamorphism, geochemistry, and origin. *American Mineralogist*, *90*, 1473–1499.

Klein, C., & Beukes, N. (1993). Sedimentology and geochemistry of the glaciogenic late proterozoic rapitan iron-formation in Canada. *Economic Geology*, *88*, 542–565.

Kopp, R., Kirschvink, J., Hilburn, I., & Nash, C. (2005). The Paleoproterozoic snowball Earth: a climate disaster triggered by the evolution of oxygenic

photosynthesis. *Proceedings of the National Academy of Sciences of the United States of America*, *102*, 11131–11136.
Kowalewski, M., & Rimstidt, J. (2003). Average lifetime and age spectra of detrital grains: toward a unifying theory of sedimentary particles. *Journal of Geology*, *111*, 427–439.
Kump, L. (2008). The rise of atmospheric oxygen. *Nature*, *451*, 277–278.
Kump, L., & Barley, M. (2007). Increased subaerial volcanism and the rise of atmospheric oxygen 2.5 billion years ago. *Nature*, *448*, 1033–1036.
Kump, L., & Garrels, R. (1986). Modeling atmospheric O2 in the global sedimentary redox cycle. *American Journal of Science*, *286*, 337–360.
Kuntz, L., Laakso, T., Schrag, D., & Crowe, S. (2015). Modeling the carbon cycle in Lake Matano. *Geobiology*, *13*, 454–461.
Laakso, T., & Schrag, D. (2014). Regulation of atmospheric oxygen during the Proterozoic. *Earth & Planetary Science Letters*, *388*, 81–91.
Lalonde, S., & Konhauser, K. (2015). Benthic perspective on Earth's oldest evidence for oxygenic photosynthesis. *Proceedings of the National Academy of Sciences of the United States of America*, *112*, 995–1000.
Lasaga, A., & Ohmoto, H. (2002). The oxygen geochemical cycle: dynamics and stability. *Geochimica Cosmochimica Acta*, *66*, 361–381.
Lenton, T., Dahl, T., Daines, S., Mills, B., Ozaki, K., Saltzman, M., & Porada, P. (2016). Earliest land plants created modern levels of atmospheric oxygen. *Proceedings of the National Academy of Sciences of the United States of America*, *113*, 9704–9709.
Li, Z., & Lee, C. (2004). The constancy of upper mantle fO2 through time inferred from V/Sc ratios in basalts. *Earth & Planet Science Letters*, *228*, 483–493.
Logan, G., Hayes, J., Hieshima, G., & Summons, R. (1995). Terminal Proterozoic reorganization of biogeochemical cycles. *Nature*, *376*, 53–56.
Lyons Reinhard, C., & Planavsky, N. (2014). The rise of oxygen in Earth's early ocean and atmosphere. *Nature*, *506*, 307–315.
Millero, F., Hubinger, S., Fernandez, M., & Garnett, S. (1987a). Oxidation of H2S in seawater as a function of temperature, pH, and ionic strength. *Environmental Science & Technology*, *21*, 439–443.
Millero, F., Sototlongo, S., & Izaguirre, M. (1987b). The oxidation kinetics of Fe(II) in seawater. *Geochimica Cosmochimica Acta*, *51*, 793–801.
Partin, C., Bekker, A., Planavsky, N., Scott, C., Gill, B., Li, C., Podkovyrov, V., Maslov, A., Konhauser, K., Lalonde, S., Love, G., Poulton, S., & Lyons, T. (2013). Large-scale fluctuations in Precambrian atmospheric and oceanic oxygen levels from the record of U in shales. *Earth and Planetary Science Letters*, *369–370*, 284–293.
Pavlov, A., Brown, L., & Kasting, J. (2001). UV shielding of NH_3 and O_2 by organic hazes in the Archean atmosphere. *Journal of Geophysical Research*, *106*, 23267–23287.
Pavlov, A., & Kasting, J. (2002). Mass-independent fractionation of sulfur isotopes in archean sediments: strong evidence for an anoxic archean atmosphere. *Astrobiology*, *2*, 27–41.
Planavsky, N., McGoldrick, P., Scott, C., Li, C., Reinhard, C., Kelly, A., Chu, X., Bekker, A., Love, G., & Lyons, T. (2011). Widespread iron-rich conditions in the mid-Proterozoic ocean. *Nature*, *477*, 448–451.
Planavsky, N., Reinhard, C., Wang, X., Thomson, D., McGoldrick, P., Rainbird, R., Johnson, T., Fischer, W., & Lyons, T. (2014). Low Mid-Proterozoic atmospheric oxygen levels and the delayed rise of animals. *Science*, *346*, 635–638.
Planavsky, N., Rouxel, O., Bekker, A., Lalonde, S., Konhauser, K., Reinhard, C., & Lyons, T. (2010). The evolution of the marine phosphate reservoir. *Nature*, *467*, 1088–1090.
Pope, E., Bird, D., & Rosing, M. (2012). Isotope composition and volume of Earth's early oceans. *Proceedings of the National Academy of Sciences of the United States of America*, *109*, 4371–4376.
Poulton, S., & Canfield, D. (2011). Ferruginous conditions: a dominant feature of the ocean through Earth's history. *Elements*, *7*, 107–112.
Poulton, S., Fralick, P., & Canfield, D. (2010). Spatial variability in oceanic redox structure 1.8 billion year ago. *Nature Geoscience*, *3*, 486–490.
Prokoph, A., Shields, G., & Veizer, J. (2008). Compilation and time-series analysis of a marine carbonate $\delta^{18}O$, $\delta^{13}C$, $^{87}Sr/^{86}Sr$ and $\delta^{34}S$ database through Earth history. *Earth-Science Reviews*, *87*, 113–133.
Raiswell, R., Reinhard, C., Derkowski, A., Owens, J., Bottrell, S., Anbar, A., & Lyons, T. (2011). Formation of syngenetic and diagenetic iron minerals in the late Archean Mt. McRae Shale, Hamersley Basin, Australia: new insights on the patterns, controls and paleoenvironmental implications of authigenic mineral formation. *Geochimica et Cosmochimica Acta*, *75*, 1072–1087.
Rasmussen, B., Fletcher, I., Brocks, J., & Kilburn, M. (2008). Reassessing the first appearance of eukaryotes and cyanobacteria. *Nature*, *455*, 1101–1104.
Reeburgh, W. (2007). Oceanic methane biogeochemistry. *Chemical Reviews*, *107*, 486–513.
Reinhard, C., Planavsky, N., Robbins, L., Partin, C., Gill, B., Lalonde, S., Bekker, A., Konhauser, K., & Lyons, T. (2013). Proterozoic ocean redox and biogeochemical stasis. *Proceedings of the National Academy of Sciences of the United States of America*, *110*, 5357–5362.
Rickard, D., & Luther, G. III (2007). Chemistry of iron sulfides. *Chemical Reviews*, *107*, 514–562.
Rye, R., & Holland, H. (1998). Paleosols and the evolution of atmospheric oxygen: a critical review. *American Journal of Science*, *298*, 621–672.
Sahoo, S., Planavsky, N., Kendall, B., Wang, X., Shi, X., Scott, C., Anbar, A., Lyons, T., & Jiang, G. (2012). Ocean oxygenation in the wake of the Marinoan glaciation. *Nature*, *489*, 546–549.
Schrag, D., Higgins, J., Macdonald, F., & Johnston, D., (2013). Authigenic Carbonate and the History of the Global Carbon Cycle. *Science*, *339*, 540–543.
Scott, A., & Glasspool, I. (2006). The diversification of Paleozoic fire systems and fluctuations in atmospheric oxygen concentration. *Proceedings of the National Academy of Sciences of the United States of America*, *103*, 10861–10865.
Shen, Y., Canfield, D., & Knoll, A. (2002). Middle proterozoic ocean chemistry: evidence from the Mcarthur basin, northern Australia. *American Journal of Science*, *302*, 81–109.
Sperling, E., Wolock, C., Morgan, A., Gill, B., Kunzmann, M., Halverson, G., Macdonald, F., Knoll, A., & Johnston, D. (2015). Statistical analysis of iron geochemical data suggests limited late Proterozoic oxygenation. *Nature*, *523*, 451–454.
Turcotte, D. (1980). On the thermal evolution of the Earth. *Earth and Planetary Science Letters*, *48*, 53–58.
Veizer, J. (1978). Secular variations in the composition of sedimentary carbonate rocks: II. Fe, Mn, Ca, Mg, Si and minor constituents. *Precambrian Research*, *6*, 381–413.
Walker, J., Hays, B., & Kasting, J. (1981). A negative feedback mechanism for the long-term stabilization of Earth's surface temperature. *Journal of Geophysical Research*, *86*, 9776–9782.
Walling, D., & Moorehead, P. (1989). The particle size characteristics of fluvial suspended sediment: an overview. *Hydrobiologia*, *176–177*, 125–149.
Westrich, J., & Berner, R. (1984). The role of sedimentary organic matter in bacterial sulfate reduction: the G model tested. *Limnology and Oceanography*, *29*, 236–249.
Zeebe, R., & Wolf-Gladrow, D. (2001). *CO_2 in seawater: equilibrium, kinetics*. Elsevier, Amsterdam: Isotopes.

SUPPORTING INFORMATION

Additional Supporting Information may be found online in the supporting information tab for this article.

How to cite this article: Laakso TA, Schrag DP. A theory of atmospheric oxygen. *Geobiology*. 2017;15:366–384. https://doi.org/10.1111/gbi.12230